J. Fluid Mech. (2012), *vol.* 712, *pp.* 327–353. © Cambridge University Press 2012
doi:10.1017/jfm.2012.422

Ageostrophic instability in rotating shallow water

Peng Wang[1]†, **James C. McWilliams**[1] **and Ziv Kizner**[2]

[1] Department of Atmospheric and Oceanic Sciences, University of California, Los Angeles, CA 90095-1565, USA

[2] Departments of Physics and Mathematics, Bar-Ilan University, Ramat-Gan 52900, Israel

(Received 11 November 2011; revised 23 April 2012; accepted 17 August 2012; first published online 28 September 2012)

Linear instabilities, both momentum-balanced and unbalanced, in several different $\overline{u}(y)$ shear profiles are investigated in the rotating shallow water equations. The unbalanced instabilities are strongly ageostrophic and involve inertia–gravity wave motions, occurring only for finite Rossby (Ro) and Froude (Fr) numbers. They serve as a possible route for the breakdown of balance in a rotating shallow water system, which leads the energy to cascade towards small scales. Unlike previous work, this paper focuses on general shear flows with non-uniform potential vorticity, and without side or equatorial boundaries or vanishing layer depth (frontal outcropping). As well as classical shear instability among balanced shear wave modes (i.e. B–B type), two types of ageostrophic instability (B–G and G–G) are found. The B–G instability has attributes of both a balanced shear wave mode and an inertia–gravity wave mode. The G–G instability occurs as a sharp resonance between two inertia–gravity wave modes. The criterion for the occurrence of the ageostrophic instability is associated with the second stability condition of Ripa (1983), which requires a sufficiently large local Froude number. When Ro and especially Fr increase, the balanced instability is suppressed, while the ageostrophic instabilities are enhanced. The profile of the mean flow also affects the strength of the balanced and ageostrophic instabilities.

Key words: instability, jets, shallow water flows

1. Introduction

Large-scale flows in the ocean are strongly influenced by the rotation ($f \neq 0$) and stable stratification ($N > 0$), and are mostly geostrophic and hydrostatic in momentum balance. They have a small Rossby number Ro and Froude number Fr, where $Ro = U/fL$ and $Fr = U/NH$. They are called 'balanced' motions and belong to the 'slow manifold' of advection and potential vorticity dynamics. The 'balanced' motions exist in the quasi-geostrophic regime ($Ro \to 0$), while at finite Ro, they satisfy a higher-order momentum balance. In contrast, the 'fast manifold', which does not satisfy balanced equations, is categorized as 'unbalanced' motions, whose primary paradigm is inertia–gravity waves. Through classical barotropic and baroclinic instabilities, the large-scale flows generate mesoscale eddies which evolve in an essentially balanced way, even at finite Ro. However, most of the energy is inhibited from transferring towards smaller scales due to the 'inverse cascade' of geostrophic

† Email address for correspondence: pengwang@atmos.ucla.edu

https://doi.org/10.1017/jfm.2012.422 Published online by Cambridge University Press

turbulence. On the other hand, kinetic energy dissipation is only effective at very small scales. Therefore, identifying the way in which balance breaks down, leading to a turbulent energy cascade towards small scales, is a fundamental geophysical fluid-dynamical issue. Several possible ways have been learnt from past work. With a strong buoyancy flux out of the ocean surface, the fluid can be gravitationally unstable (Chandrasekhar 1961), where convection starts and increases the mixing. Centrifugal instability (Ooyama 1966) occurs where the Ertel potential vorticity changes sign; it greatly enhances local vertical motions. Kelvin–Helmholtz instability starts when there is strong vertical shear in a stratified flow, and it induces vertical overturning. When flow passes over the oceanic bottom topography, the internal waves generated can propagate away from the flow and break near the coast. The examples discussed above are efficient ways of transferring energy from balanced to unbalanced motions. However, most of these situations occur in the planetary boundary layer, the coastal region, or the bottom of the ocean. The interior region occupies a larger volume than the boundary regions, but the process for the breakdown of balance and forward energy cascade in the interior ocean is much less well known. Is there a more general route for the breakdown of balance in an interior flow? Ageostrophic instability is one possible answer to the question. Some previous literature (Griffiths, Killworth & Stern 1982; Boss, Paldor & Thompson 1996) describes 'ageostrophic' as the finite Ro effect for a higher-order balanced instability. Our main focus is the ageostrophic instability that is unbalanced, the energy of which may be efficiently transferred to small scales in a turbulent regime.

McWilliams *et al.* (1998) proposed three sufficient conditions for the breakdown of balanced evolution in a three-dimensional stratified flow: (i) sign change of stratification N^2 (related to gravitational instability); (ii) sign change of A, the absolute vorticity in isentropic coordinates, which is proportional to the Ertel potential vorticity (related to the centrifugal instability); and (iii) sign change of $A - S$, where S is the horizontal strain rate in isentropic coordinates. The third criterion can be satisfied in more common situations than the first two, in the sense that it only requires a moderate but finite magnitude Ro. Several three-dimensional instability problems have been solved to study the relevance of the third criterion (McWilliams & Yavneh 1998; Yavneh, McWilliams & Molemaker 2001; Molemaker, McWilliams & Yavneh 2001; McWilliams 2003; McWilliams & Molemaker 2004; Molemaker & McWilliams 2005; Ménesguen, McWilliams & Molemaker 2012), and ageostrophic instabilities are found in association with the $A - S$ criterion, which is called anticyclonic ageostrophic instability (A tends to be small in anticyclonic flows). In all cases the unstable modes have a fully three-dimensional structure. Bouchut, Ribstein & Zeitlin (2011) study a barotropic Bickley jet in a two-layer shallow water model and find a baroclinic ageostrophic instability when the inertial instability joins with the barotropic instability. This instability might be related to the above conditions but it would not occur in a single-layer model. Ripa (1983) proposed two stability conditions in rotating shallow water equations. His first condition is related to Rayleigh's inflection point criterion (relevant to the barotropic instability), and the second one refers to a local Froude number condition. Within the theoretical framework discussed above, the $A - S$ condition (McWilliams *et al.* 1998) and Froude number condition (Ripa 1983) are mostly likely to be related to ageostrophic instability in rotating shallow water. One of our objectives is to investigate the criterion for the occurrence of ageostrophic instability and its associated physical interpretation.

https://doi.org/10.1017/jfm.2012.422 Published online by Cambridge University Press

Several types of instability have been identified in the shallow water equations in previous work. Classical (barotropic) shear instability has been well described by Poulin & Flierl (2003) and Perret, Dubos & Stegner (2011). Both geostrophic and ageostrophic instabilities are found in a geostrophic surface-frontal flow, that is, a flow with a vanishing layer depth where the bounding interface 'outcrops' (and quasi-geostrophic theory based on $Ro, Fr \to 0$ fails). The frontal-trapped mode is stable in a one-layer shallow water frontal flow with uniform potential vorticity (Paldor 1983). With another nearby front or non-uniform potential vorticity in the flow, the frontal mode becomes unstable, by interacting with another frontal mode or the shear mode (Griffiths *et al.* 1982; Kubokawa 1985). With a nearby side boundary, the interaction of the frontal-trapped mode and the coastal-trapped mode (Kelvin wave mode) leads to an ageostrophic instability (Kubokawa 1986; Gula & Zeitlin 2010). With the addition of an active second layer, the frontal flow has non-uniform potential vorticity, and the frontal mode, the shear mode, and the gravity wave mode lead to different combinations of resonance with several types of instability (Killworth, Paldor & Stern 1984; Boss *et al.* 1996; Gula, Zeitlin & Bouchut 2010). In a non-rotating shallow water model, Satomura (1980) and Balmforth (1999) studied wall-bounded flows (a Couette flow with zero potential-vorticity gradient and a hyperbolic tangent flow with small potential-vorticity gradient, respectively), suggesting that there is an instability when the gravity waves resonate. Dritschel & Vanneste (2006) examined a geostrophic potential vorticity front and found a weakly unstable ageostrophic mode that is associated with the potential vorticity discontinuity and far-field inertia–gravity waves. Hayashi & Young (1987) demonstrated a type of ageostrophic instability triggered by the resonance between two Kelvin waves in an equatorial flow with zero potential vorticity. Sakai (1989) and Gula, Plougonven & Zeitlin (2009) found a type of instability caused by a resonance between a shear wave and a boundary Kelvin wave in a channelled, two-layer hydrostatic model. These shallow water studies of ageostrophic instability have special 'edges', with either boundaries, the equator, surface outcropping, or singularity in the potential vorticity gradient, which support particular neutral mode types (e.g. Kelvin wave, frontal wave, boundary-trapped wave, singularity-trapped wave), and hence potentially have special resonant instabilities. Our work aims to study generic ageostrophic instabilities in more general mean flows, which can provide a comprehensive guide to understanding the possible breakdown of balance processes in a horizontal interior shear.

This paper solves the linear instability problem in a single-layer, uniformly rotating (non-equatorial) shallow water model for several balanced mean shear profiles $\overline{u}(y)$ with a continuous, non-uniform potential vorticity, and without side boundaries or vanishing layer depth. Because there is no interior stratification and the horizontal velocity is depth-independent in this model, the baroclinic (balanced), gravitational, centrifugal, and Kelvin–Helmholtz instabilities do not occur. We are searching for the generic type of ageostrophic instability, the criterion for its occurrence, and the associated dynamical mechanism. In § 2 we specify the equations, the non-dimensional parameters, and the mean flows. A general picture of the neutral and unstable modes is shown in § 3, followed by a detailed study of each type of instability in §§ 4 and 5. In § 6 we examine *Ro* and *Fr* dependence, the degree of ageostrophy, and the energy diagnostics for the instabilities. A nonlinear example of the ageostrophic instability is shown in § 7. The paper summarizes with a discussion in § 8.

https://doi.org/10.1017/jfm.2012.422 Published online by Cambridge University Press

2. Shallow water equations and mean flows

We study the instability problem in an f-plane rotating conservative shallow water model, with dimensional equations

$$\begin{cases} \dfrac{\partial u}{\partial t} + u\dfrac{\partial u}{\partial x} + v\dfrac{\partial u}{\partial y} - fv + g'\dfrac{\partial h}{\partial x} = 0, \\ \dfrac{\partial v}{\partial t} + u\dfrac{\partial v}{\partial x} + v\dfrac{\partial v}{\partial y} + fu + g'\dfrac{\partial h}{\partial y} = 0, \\ \dfrac{\partial h}{\partial t} + \dfrac{\partial (uH)}{\partial x} + \dfrac{\partial (vH)}{\partial y} = 0, \end{cases} \tag{2.1}$$

where f is the Coriolis frequency, g' is the reduced gravity, $H = H_0 + h$ is the total water depth, with H_0 the average value, h is the surface elevation, and u and v are zonal and meridional velocities, respectively. The equations can be non-dimensionalized to yield two independent parameters, Rossby number Ro and Froude number Fr:

$$Ro = \frac{U_0}{fL}, \quad Fr = \frac{U_0}{\sqrt{g'H_0}}, \tag{2.2}$$

where U_0 is the velocity scale of the mean flow and L is the horizontal scale of the mean shear. We decompose the variables into the mean parallel flow and the fluctuations:

$$u = \overline{u}(y) + u'(x, y, t), \quad v = v'(x, y, t), \quad h = \overline{h}(y) + h'(x, y, t). \tag{2.3}$$

The non-dimensional linearized fluctuation equations are

$$\begin{cases} Ro\left(\dfrac{\partial u'}{\partial t} + \overline{u}\dfrac{\partial u'}{\partial x} + v'\dfrac{\partial \overline{u}}{\partial y}\right) - v' + \dfrac{\partial h'}{\partial x} = 0, \\ Ro\left(\dfrac{\partial v'}{\partial t} + \overline{u}\dfrac{\partial v'}{\partial x}\right) + u' + \dfrac{\partial h'}{\partial y} = 0, \\ Fr^2\left(\dfrac{\partial h'}{\partial t} + \overline{u}\dfrac{\partial h'}{\partial x} + v'\dfrac{\partial \overline{h}}{\partial y}\right) + (Ro + Fr^2\overline{h})\left(\dfrac{\partial u'}{\partial x} + \dfrac{\partial v'}{\partial y}\right) = 0, \end{cases} \tag{2.4}$$

with the mean flow in geostrophic balance, $\overline{u} = -\mathrm{d}\overline{h}/\mathrm{d}y$. Assuming the solutions have a form $(u', v', h') = \mathrm{Re}[(\hat{u}(y), \hat{v}(y), \hat{h}(y))\,\mathrm{e}^{\mathrm{i}(kx-\omega t)}]$, where k is the downstream (x-direction) wavenumber and ω is the wave frequency, then we have an eigenvalue problem:

$$\begin{pmatrix} kRo\overline{u} & -\mathrm{i}\left(Ro\dfrac{\partial \overline{u}}{\partial y} - 1\right) & k \\ -\mathrm{i} & kRo\overline{u} & -\mathrm{i}\dfrac{\partial}{\partial y} \\ k(Ro + Fr^2\overline{h}) & -\mathrm{i}\left(Fr^2\dfrac{\partial \overline{h}}{\partial y} + (Ro + Fr^2\overline{h})\dfrac{\partial}{\partial y}\right) & kFr^2\overline{u} \end{pmatrix} \begin{pmatrix} \hat{u} \\ \hat{v} \\ \hat{h} \end{pmatrix} = \omega \begin{pmatrix} Ro & 0 & 0 \\ 0 & Ro & 0 \\ 0 & 0 & Fr^2 \end{pmatrix} \begin{pmatrix} \hat{u} \\ \hat{v} \\ \hat{h} \end{pmatrix}. \tag{2.5}$$

Note that all the mentioned variables will be non-dimensional henceforth.

https://doi.org/10.1017/jfm.2012.422 Published online by Cambridge University Press

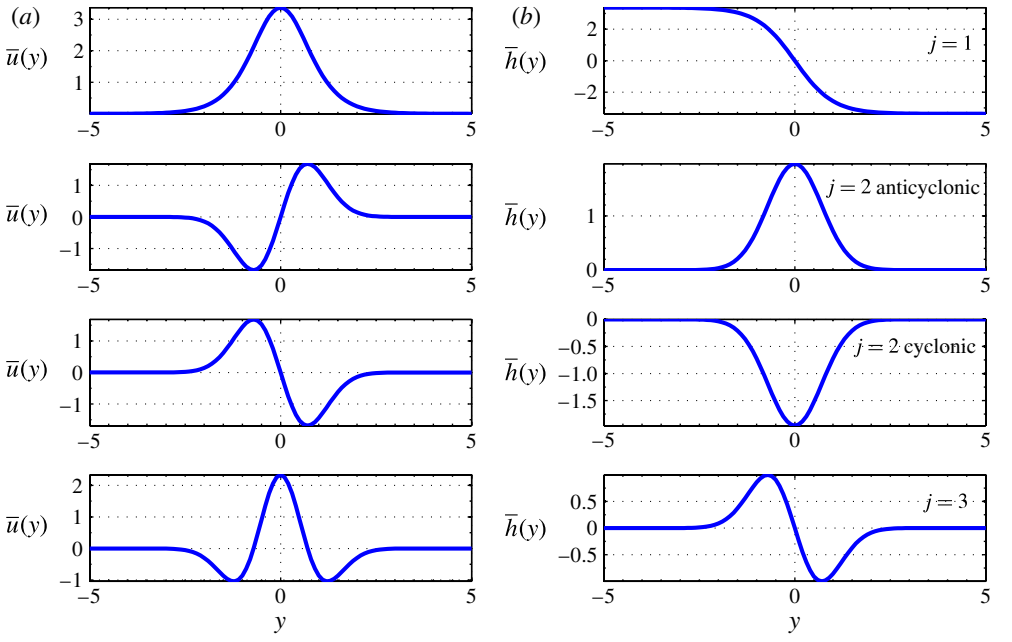


FIGURE 1. (Colour online) (*a*) Mean velocity $\overline{u}(y)$ and (*b*) geostrophic-balanced surface elevation $\overline{h}(y)$ for $j = 1, 2$ (anticyclonic), 2 (cyclonic) and 3, respectively. To normalize the mean flows, we choose $\overline{h}_{max} = 1$ in $j = 3$, and all the mean flows have the same $\overline{u}_{max} - \overline{u}_{min}$ value.

We examine four types of mean flow: the Bickley jet ($j = 1$), the cyclonic and anticyclonic double jet ($j = 2$), and the triple jet ($j = 3$), whose analytical forms are

$$\begin{aligned} &\overline{u} = A_1 \cosh^{-2} y && (j = 1), \\ &\overline{u} = -A_2 y\, \mathrm{e}^{-y^2} \quad \text{or} \quad \overline{u} = A_2 y\, \mathrm{e}^{-y^2} && (j = 2), \\ &\overline{u} = A_3 (1 - 2y^2)\, \mathrm{e}^{-y^2} && (j = 3), \end{aligned} \tag{2.6}$$

respectively. A_1, A_2 and A_3 are positive constants. The value of A_3 is set such that $\overline{h}_{max} = 1$ in $j = 3$, and the $j = 1$ and 2 mean flows are normalized to have the same $\overline{u}_{max} - \overline{u}_{min}$ by adjusting the value of A_1 and A_2. The $\overline{u}(y)$ and $\overline{h}(y)$ mean profiles are shown in figure 1. The $j = 3$ mean flow is more general in the sense that it contains a Bickley jet in the centre, an anticyclonic shear on the left, and a cyclonic shear on the right. The total water depth should be positive, which implies a limitation of the existence of the mean flow (which has $\overline{h}_{min} < 0$) in the (Ro, Fr) space. The condition $H = H_0 + \overline{h}^* > 0$ (where * denotes dimensional variables) implies $(Fr^2/Ro)|\overline{h}_{min}| \leqslant 1$, so the limitation condition is $Fr^2 \leqslant \lambda Ro$ for the mean flows. The value of λ depends on the particular mean flow: $\lambda = 0.2968$ for $j = 1$, $\lambda = 0.5098$ for $j = 2$ cyclonic, and $\lambda = 1$ for $j = 3$. This limitation does not apply to the $j = 2$ anticyclonic shear, where it always satisfies $H = H_0 + \overline{h}^* > 0$. Figure 2 shows the $\overline{q}(y)$ profiles of the mean flows for small (*a–d*) and moderate (*e–h*) Ro,

https://doi.org/10.1017/jfm.2012.422 Published online by Cambridge University Press

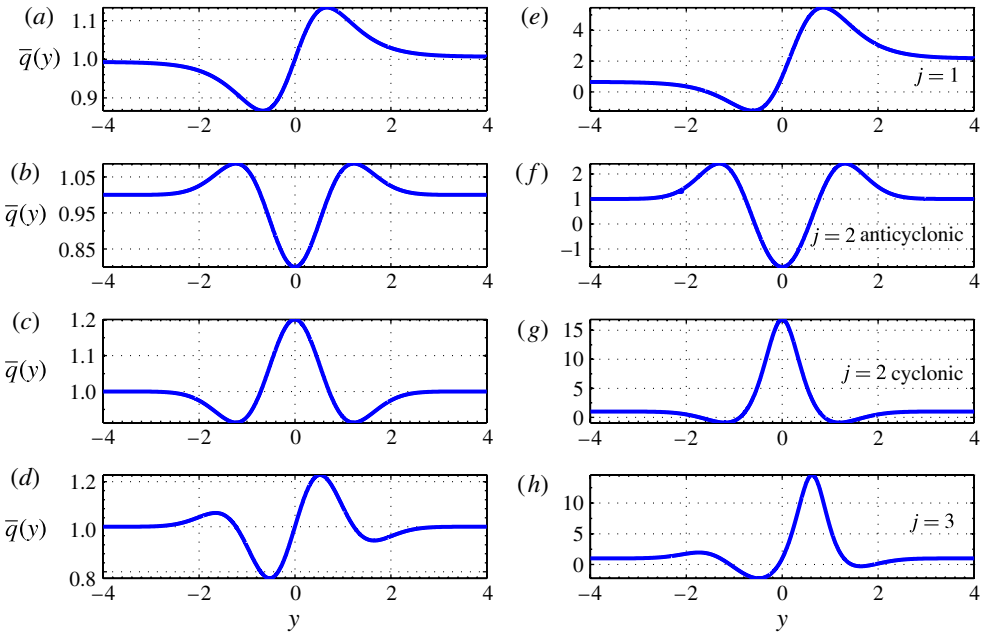


FIGURE 2. (Colour online) Mean potential vorticity $\overline{q}(y)$ for (*a*,*e*) $j = 1$, (*b*,*f*) $j = 2$ (anticyclonic), (*c*,*g*) $j = 2$ (cyclonic) and (*d*,*h*) $j = 3$. The small Ro ($= 0.05$) profiles are shown in (*a*)–(*d*) and the finite Ro ($=1$) profiles are shown in (*e*)–(*h*). (*a–d*) $Ro = 0.05$, $Fr = 0.01$; (*e*) $Ro = 1$, $Fr = 0.4$; (*f*,*g*) $Ro = 1$, $Fr = 0.6$; (*h*) $Ro = 1$, $Fr = 0.8$.

where

$$\overline{q} = \frac{1 - Ro\,\overline{u}_y}{1 + \dfrac{Fr^2}{Ro}\overline{h}}. \tag{2.7}$$

For small Ro and Fr (quasi-geostrophic regime), the water depth is nearly constant in y. The magnitude of $\overline{q}$ is symmetric for the regions with $\overline{h} > 0$ and $\overline{h} < 0$, and its value is small. For moderate Ro and Fr, the surface elevation becomes comparable to the average water depth. Further, $\overline{h} > 0$ has a small effect on $\overline{q}$ (figure 2*f*), while in the $\overline{h} < 0$ region, $\overline{q}$ has a large value due to the thin water depth (figure 2*e,g,h*). For a fixed Ro, increasing Fr leads to a significant increase of the local $\overline{q}$ in the $\overline{h} < 0$ region (not shown).

It has been identified that three types of solution coexist in a $\overline{u}(y)$ flow: the conjugate pairs of growing and decaying modes, the non-singular neutral mode, and the singular continuum mode (Lin 1961; Held 1985). In shallow water equations, the eigenvalue problem can be expressed by $\boldsymbol{A\phi} = \omega\boldsymbol{B\phi}$, where $\boldsymbol{A}$ and $\boldsymbol{B}$ are real matrices,

$$\boldsymbol{A} = \begin{pmatrix} kRo\,\overline{u} & -\left(Ro\dfrac{\partial \overline{u}}{\partial y} - 1\right) & k \\ 1 & k\,Ro\,\overline{u} & \dfrac{\partial}{\partial y} \\ k(Ro + Fr^2\,\overline{h}) & -\left(Fr^2\dfrac{\partial \overline{h}}{\partial y} + (Ro + Fr^2\,\overline{h})\dfrac{\partial}{\partial y}\right) & kFr^2\,\overline{u} \end{pmatrix}, \tag{2.8}$$

https://doi.org/10.1017/jfm.2012.422 Published online by Cambridge University Press

$$\boldsymbol{B} = \begin{pmatrix} Ro & 0 & 0 \\ 0 & Ro & 0 \\ 0 & 0 & Fr^2 \end{pmatrix}, \tag{2.9}$$

and $\boldsymbol{\phi} = (\hat{u}, \mathrm{i}\hat{v}, \hat{h})^{\mathrm{T}}$, with $^{\mathrm{T}}$ denoting the transpose. If ω and $\boldsymbol{\phi}$ are its eigenvalue and eigenfunction, then according to $(\boldsymbol{A\phi})^* = \boldsymbol{A\phi}^* = (\omega \boldsymbol{B\phi})^* = \omega^* \boldsymbol{B\phi}^*$, ω^* and $\boldsymbol{\phi}^*$ are its eigenvalue and associated eigenfunction, respectively, where * denotes the complex conjugate. Therefore, the growing and decaying modes appear in pairs in the non-viscous case. For the $j = 2$ mean flows, another symmetry appears because $\overline{u}(y) = -\overline{u}(-y)$ and $\overline{h}(y) = \overline{h}(-y)$. We have $\boldsymbol{A}(y)\boldsymbol{\phi} = \omega \boldsymbol{B\phi}$, where $\boldsymbol{\phi} = (\hat{u}(y), \mathrm{i}\hat{v}(y), \hat{h}(y))^{\mathrm{T}}$. Let $y \to -y$ and take the conjugate of the whole equation; it follows that $\boldsymbol{A}(y)\tilde{\boldsymbol{\phi}} = (-\omega^*)\boldsymbol{B}\tilde{\boldsymbol{\phi}}$, where $\tilde{\boldsymbol{\phi}} = (\hat{u}^*(-y), -\mathrm{i}\hat{v}^*(-y), -\hat{h}^*(-y))^{\mathrm{T}}$. A new symmetric eigenvalue $-\omega^*$ and associated eigenfunction are obtained. This means that the growing (or decaying) modes can be found in pairs (ω and $-\omega^*$), with the same growth rate and opposite-signed phase speeds, and their associated eigenfunctions $\boldsymbol{\phi}$ and $\tilde{\boldsymbol{\phi}}$ are partially symmetric and partially anti-symmetric in y. The paired unstable modes in $j = 2$ flows will be shown in § 3. Besides the growing and decaying pairs, neutral mode solutions also exist for the equations, which can become unstable when they couple and interact (§ 3).

To solve the eigenvalue problem, we use an eigensolver with the Fortran library ARPACK. Because a large resolution is needed for an accurate solution, it is too expensive to compute the full-spectrum eigenvalues. ARPACK computes a few eigenvalues and corresponding eigenfunctions close to the given 'target' (guessed eigenvalue) by an iterative convergence process. The result is checked with a linear time integration code. We discretize the differential operators by a second-order centred finite-difference method, in a staggered grid, with a resolution of $N \sim 5000$ in the y direction. The domain in the computation is sufficiently large ($[-5\,5]$) to remove the boundary influence on the unstable modes, which are trapped in the mean shear region. The boundary condition at $y = \pm 5$ is chosen to be $v' = 0$ and $\partial u'/\partial y = \partial h'/\partial y = 0$. We do not look for radiating instabilities by setting a matching boundary condition, therefore none of the unstable modes found by our eigensolver propagate along y. We check our result by increasing resolution in both grids and k until the eigenvalue converges and no longer changes with higher resolution. The eigenvalues converge well for our current resolution. For most of our numerical results, viscosity terms ($Ek\nabla^2 u$, $Ek\nabla^2 v$) are not needed (Ek is the Ekman number). However, there is a viscosity option in order to eliminate the unreliable eigenmodes that are marginally resolved. Some weakly unstable or neutral modes with critical layers could be inaccurately determined without viscosity. On the contrary, the unstable mode, which is our focus, has an imaginary part in the eigenvalue so it can be accurately calculated by the eigensolver. We have tested different Ek values to make sure that the viscosity is sufficiently small that it has negligible effect on the unstable modes. The correctness of our eigensolver is confirmed by reproducing the growth rate of the barotropic instability in a Bickley jet (figures 2 and 3 in Poulin & Flierl 2003 and figure 2 in Lambaerts, Lapeyre & Zeitlin 2011).

3. Neutral and unstable modes

The dynamical mechanism of instability has been commonly interpreted in previous literature as a resonant coupling of two neutral waves (Hayashi & Young 1987;

https://doi.org/10.1017/jfm.2012.422 Published online by Cambridge University Press

Sakai 1989; Gula & Zeitlin 2010). In the general cases we investigate, this interpretation is helpful for us in understanding the unstable modes, especially the ageostrophic modes, so this conventional concept is kept in this paper. The neutral wave modes are Doppler-shifted and modified by the background mean shear, with both frequency and mode structure being changed. When two neutral wave modes have the same frequency, they can interact and resonate with each other, leading to an instability.

3.1. *Neutral modes*

In rotating shallow water equations, there are mainly two types of non-singular neutral wave modes in an interior shear flow that does not have side boundaries or surface outcropping: the shear wave mode and the inertia–gravity wave mode. The shear wave mode (also called the 'Rossby wave' or 'vortical wave') is defined as the mode that exists due to the potential vorticity gradient. It is a balanced mode, which can be found in the quasi-geostrophic equations. For a finite Ro where quasi-geostrophy fails, the shear wave mode may satisfy a higher-order balanced dynamics (§ 1). We refer to the balanced shear wave mode as the B mode.

To estimate the phase speed of the shear wave, we start from the f-plane quasi-geostrophic free-surface potential vorticity equation,

$$\frac{\mathrm{D}q_{QG}}{\mathrm{D}t} = 0, \quad q_{QG} = \nabla^2\psi - \frac{Fr^2}{Ro^2}\psi, \tag{3.1}$$

where ψ is the stream function with $\boldsymbol{u} = \hat{\boldsymbol{z}} \times \boldsymbol{\nabla}\psi$. The quasi-geostrophic potential vorticity equation follows from (2.1), by taking Ro and Fr to zero limit as their ratio remains constant. The linearized potential vorticity equation is

$$\left(\frac{\partial}{\partial t} + \overline{u}\frac{\partial}{\partial x}\right)\left(\nabla^2\psi' - \frac{Fr^2}{Ro^2}\psi'\right) + \frac{\partial\psi'}{\partial x}\left(\frac{Fr^2}{Ro^2}\overline{u} - \overline{u}_{yy}\right) = 0. \tag{3.2}$$

With the assumption $\psi' = \mathrm{Re}[\Psi(y)\,\mathrm{e}^{\mathrm{i}(kx-\omega t)}]$, we get

$$\Psi_{yy} + \left[\frac{\mathrm{d}\overline{q}_{QG}/\mathrm{d}y}{\overline{u}-c} - \left(k^2 + \frac{Fr^2}{Ro^2}\right)\right]\Psi = 0, \quad \frac{\mathrm{d}\overline{q}_{QG}}{\mathrm{d}y} = \frac{Fr^2}{Ro^2}\overline{u} - \overline{u}_{yy}. \tag{3.3}$$

To make a local estimate for the neutral mode, we assume $\mathrm{d}\overline{q}_{QG}/\mathrm{d}y$ and $\overline{u}$ are constant at local y, and hence $\Psi(y)$ has a form of $\mathrm{e}^{\mathrm{i}ly}$. Then the estimated phase speed for the balanced shear wave mode becomes

$$C_{QG} = \overline{u} - \frac{\mathrm{d}\overline{q}_{QG}/\mathrm{d}y}{k^2 + l^2 + \dfrac{Fr^2}{Ro^2}}. \tag{3.4}$$

The locally estimated phase speed of the shear wave shows, that beyond the Doppler shift of the mean velocity, its sign is opposite to the sign of the potential vorticity gradient. The mathematical expression of the phase speed becomes complicated with a finite Ro effect, but we expect its dependence on $\overline{u}$ and $\overline{q}_y$ to remain qualitatively the same for the B mode, where

$$\frac{\mathrm{d}\overline{q}}{\mathrm{d}y} = \frac{\dfrac{Fr^2}{Ro}\overline{u}\,\overline{q} - Ro\overline{u}_{yy}}{1 + \dfrac{Fr^2}{Ro}\overline{h}}. \tag{3.5}$$

https://doi.org/10.1017/jfm.2012.422 Published online by Cambridge University Press

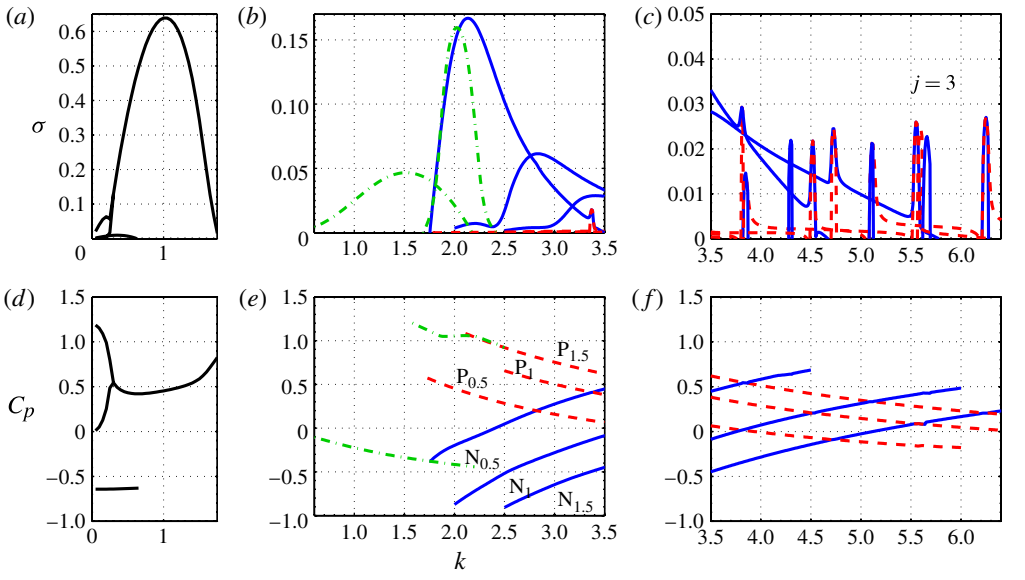


FIGURE 3. (Colour online) (*a–c*) Growth rate σ and (*d–f*) phase speed C_p for $Ro = 1.0$, $Fr = 0.99$ and $j = 3$. The black lines represent B–B modes (*a,d*). The blue solid and red dashed curves represent N and P inertia–gravity wave modes respectively. The numbers next to N or P in the legend are integers or half-integers, which denotes the wavenumbers in y. Following the N or P mode curves, the smooth σ over a wide k range presents B–G modes (*b,e*). The green dot-dashed lines are also B–G modes (*b,e*). The σ peaks at intermediate and large k, where N and P modes overlap, are G–G modes (*c,f*). All the unstable B–B and B–G modes are shown in the plot, while only a few G–G modes are presented.

The background $\overline{q}_y$ is essential for the existence of the shear wave mode. With uniform potential vorticity (Satomura 1980; Hayashi & Young 1987), there is no instability that involves a B mode. For a fixed set of (k, Ro, Fr), a singular $\overline{q}_y$ value supports a single shear wave mode. In Boss *et al.* (1996) and Dritschel & Vanneste (2006), the stepwise uniform potential vorticity creates a singular $\overline{q}_y$ at the front, which supports a B mode trapped near the singular point. In Killworth *et al.* (1984), Kubokawa (1986) and Gula & Zeitlin (2010), the surface outcropping point is singular in $\overline{q}_y$ and supports a frontal-trapped wave, which behaves the same as a B mode at small wavenumbers. If $\overline{q}_y$ is continuous in y, a set of shear wave modes with a continuous range of phase speeds coexist due to the variation of $\overline{q}_y$. Belonging to balanced dynamics, the shear wave mode has a slow phase speed comparable to $\overline{u}$ when Ro is small.

Another type of non-singular neutral mode in rotating shallow water equations is the inertia–gravity wave mode. The inertia–gravity wave velocity is highly divergent, and hence it does not exist in the quasi-geostrophic regime. The mode is unbalanced, so any instability involving this mode is an unbalanced instability. We refer to the inertia–gravity mode as the G mode. The G mode has two branches: the P mode (positive phase speed branch, red dashed lines in figure 3) and the N mode (negative phase speed branch, blue solid lines in figure 3). Without mean flow background, the dispersion relation for an inertia–gravity wave mode is

$$C_p^{\pm} = \pm\sqrt{\frac{k^2 + l^2}{Fr^2} + \frac{1}{Ro^2}}\Big/k, \tag{3.6}$$

https://doi.org/10.1017/jfm.2012.422 Published online by Cambridge University Press

where l is the wavenumber in the y direction, and C_p^+ (C_p^-) is the phase speed for the P (N) mode without mean flow. The inertia–gravity wave mode has a fast phase speed when Ro, $Fr \ll 1$. Without $\overline{u}(y)$, the phase speed of a neutral B mode and that of a neutral G mode are well separated. The Doppler shift and modification by $\overline{u}(y)$ lead to the possibility of an interaction between them.

3.2. *Unstable modes*

We find three types of unstable mode in the mean flows: B–B, B–G and G–G instability. As mentioned in § 3.1, the instabilities can be interpreted as a coupling between two neutral wave modes, so we name an instability by its resonating components. The B–B instability is the classical shear instability (barotropic instability). The B–G and G–G instabilities are two different types of ageostrophic instability. An unstable B–G mode exists at small and intermediate k (∼1–5), with attributes of both a balanced shear wave mode, and an inertia–gravity wave mode. An unstable G–G mode exists at both intermediate and large k (>3), with attributes of two inertia–gravity wave modes modified by $\overline{u}(y)$.

The growth rate σ and downstream (i.e. in the x direction) phase speed C_p versus k for the four mean flows are shown in figures 3–6. The results shown in the figures are for moderate Ro and Fr (order one). The triple jet is the most general one among the mean flows, and all three types of instability appear in this mean flow. It gives us a complete view of the instabilities for a moderate Ro and Fr, so the unstable modes of the triple jet are shown in the beginning and most of our further results are demonstrated in the triple jet. In figure 3(*a*,*d*), the black curves represent the B–B instability. In figure 3(*b*,*c*, *e*,*f*), the red dashed (P mode) and blue solid (N mode) curves are G modes. We label the G modes by P (or N) and the approximate wavenumber in y (here we use a notation m for these discrete wavenumbers), which only have integer or half-integer values. At small and intermediate k (∼1–5), the unstable red or blue modes have a smooth growth rate over a broad k band. They are a B–G instability. Although the modes shown by green dot-dashed lines (figure 3*b*,*e*) belong to neither a P nor an N group, they are also a B–G instability. The unstable modes with multiple growth rate peaks at intermediate and large k, where the P and N modes overlap, are a G–G instability. Figures 4–6 follow the same plotting convention as figure 3. Note that the y axes of the growth rate plots in figures 3, 5 and 6 are of different scales. The G–G instability is somewhat weaker than the B–B and B–G instabilities; however, its occurrence extends to very large downstream wavenumbers, and the number of the unstable G–G modes is infinite (only a few examples are shown in figures 3 and 4). In sum, both B–G and G–G modes are unbalanced modes; the former has a board band in k while the latter appears as peaks in growth rate.

B–B and B–G instabilities appear in all four types of mean flow. For moderate Ro and Fr (order one), G–G instability only occurs in $j = 2$ (cyclonic) and $j = 3$ mean flows (shown in figures 3 and 4). We do find G–G instability in $j = 2$ (anticyclonic), but for very large Ro (∼10). For $j = 1$, the G–G instability does not exist. As shown in figure 3, the balanced and ageostrophic instabilities have comparable growth rate in $j = 3$. With the same bulk $Ro = 1.0$ and $Fr = 0.7$, in $j = 2$ (cyclonic), the ageostrophic instability is dominant over the balanced instability (figure 4), while in $j = 2$ (anticyclonic), the balanced instability is dominant (figure 5). The ageostrophic instability is weak in the Bickley jet even for $Ro = 3.0$ (figure 6). As discussed in § 2, the growth rate and dispersion curves occur in symmetric pairs for $j = 2$ (figures 4 and 5): the P_m and N_m modes have the same $\sigma(k)$ curve, and their $C_p(k)$ curves are

https://doi.org/10.1017/jfm.2012.422 Published online by Cambridge University Press

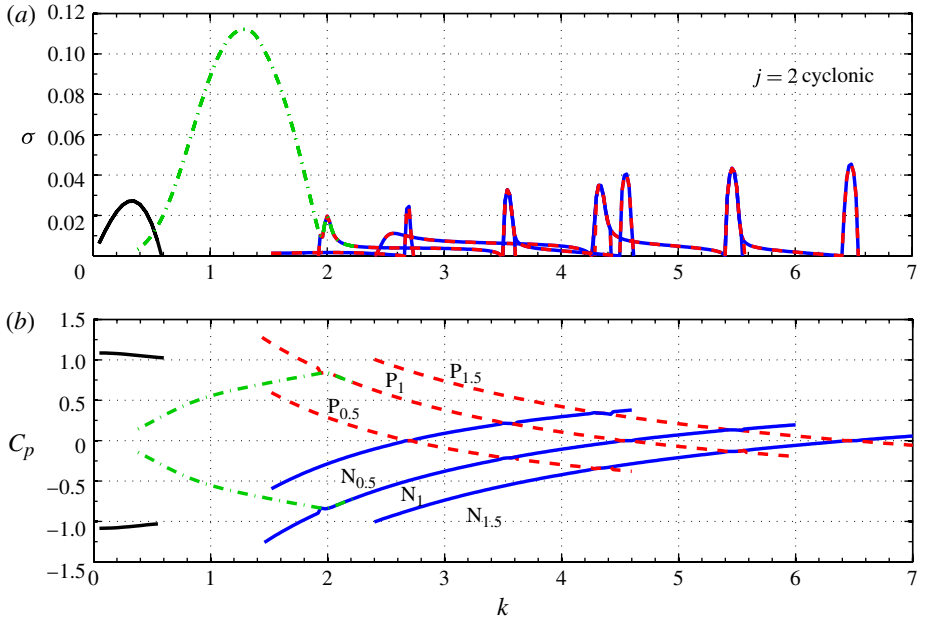


FIGURE 4. (Colour online) (*a*) Growth rate σ and (*b*) phase speed C_p plots for $Ro = 1.0$, $Fr = 0.7$ and $j = 2$ (cyclonic). Plotting conventions are the same as in figure 3. The plots contain B–B, B–G and G–G modes.

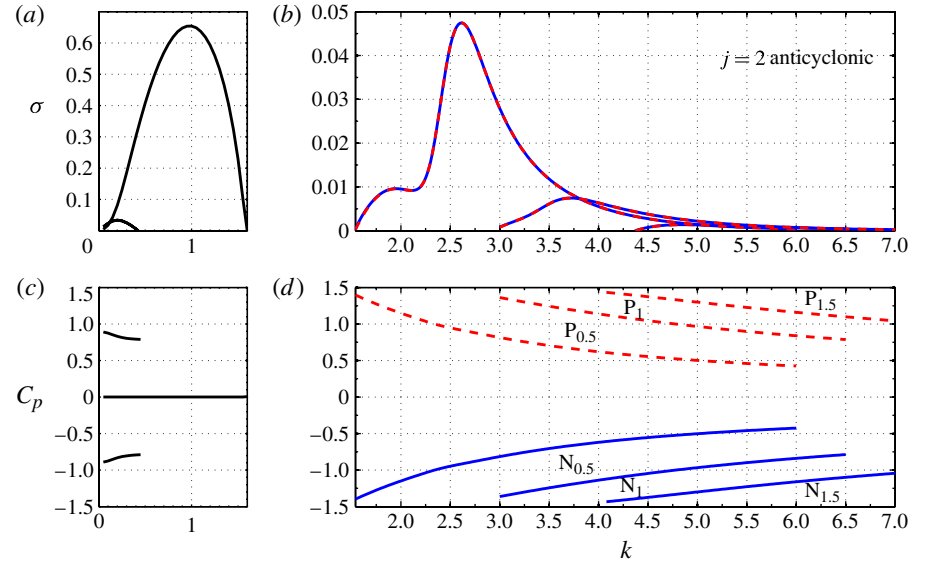


FIGURE 5. (Colour online) (*a,b*) Growth rate σ and (*c,d*) phase speed C_p plots for $Ro = 1.0$, $Fr = 0.7$ and $j = 2$ (anticyclonic). Plotting conventions are the same as in figure 3. The plots contain (*a,c*) B–B and (*b,d*) B–G modes.

symmetric around $C_p = 0$. Their corresponding eigenfunctions are symmetric (v' and h') or anti-symmetric (u') about $y = 0$.

https://doi.org/10.1017/jfm.2012.422 Published online by Cambridge University Press

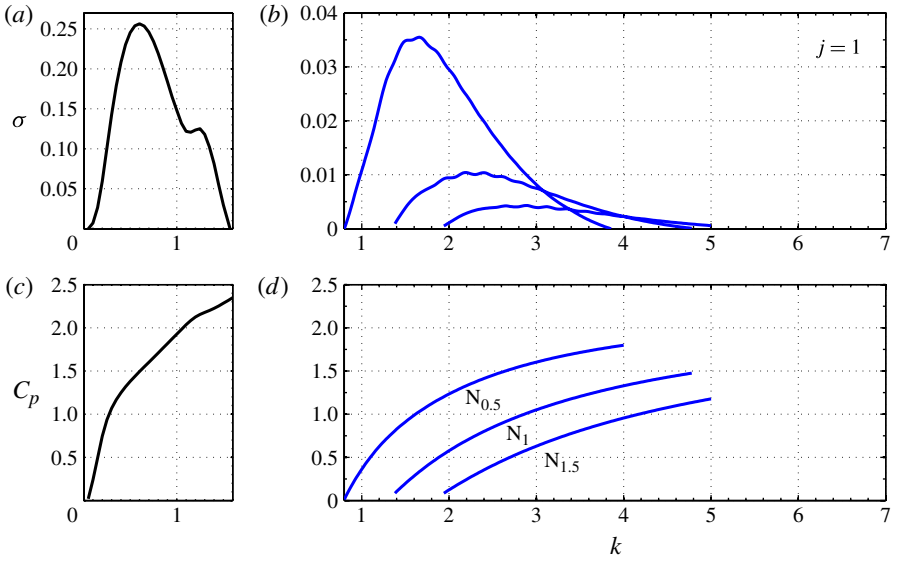


FIGURE 6. (Colour online) (*a,b*) Growth rate σ and (*c,d*) phase speed C_p plots for $Ro = 3.0$, $Fr = 0.9$ and $j = 1$. Plotting conventions are the same as in figure 3. The plots contain (*a,c*) B–B and (*b,d*) B–G modes.

4. B–B instability

The balanced (barotropic) instability (Drazin & Reid 1981; Poulin & Flierl 2003) is associated with the inflection point in the parallel mean flow, where the potential vorticity gradient changes sign (Rayleigh 1880). This instability appears at small k ($k < 2$). The growth rate is strongest at the $Fr = 0$ limit, where it is independent of Ro, and increasing Fr tends to suppress the B–B instability. Figure 7 shows the fluctuation fields of the balanced modes at a given time, for small (*a*) and intermediate (*b*) (Ro, Fr) pairs, and $j = 3$. The associated mean flow $\overline{q}_y$ profiles are shown below the fluctuation plots. For small (Ro, Fr), which is in the quasi-geostrophic regime, the field patterns are strongly geostrophic-balanced and quite symmetric in y. When (Ro, Fr) increases, the patterns are still mostly geostrophic. However, the fluctuations are no longer symmetric in y, and are mostly concentrated in the anticyclonic shear region. The magnitude of $\overline{q}_y$ becomes significantly large in the cyclonic shear region due to a strong surface depression. With a finite Ro and Fr effect, the instability of a parallel cyclonic shear weakens much more significantly than that of an anticyclonic shear (figures 4 and 5). Therefore for moderate Ro and Fr, the B–B mode in $j = 3$ occurs only in the anticyclonic shear. The study of Perret *et al.* (2011) also shows that B–B instability favours the anticyclonic shear. The B–B instability is mostly balanced, even for an intermediate Ro and Fr.

The B–B instability can be interpreted as a resonance between two oppositely propagating shear wave modes. The shear wave mode in $\overline{q}_y > 0$ region has a negative phase speed, and the shear wave mode in $\overline{q}_y < 0$ region has a positive phase speed. With the Doppler shift of the mean flow velocity, the two B modes have the same phase speed and could interact with each other. The occurrence of the instability requires that the flow has both $\overline{q}_y > 0$ and $\overline{q}_y < 0$ regions, which is consistent with Rayleigh's condition.

https://doi.org/10.1017/jfm.2012.422 Published online by Cambridge University Press

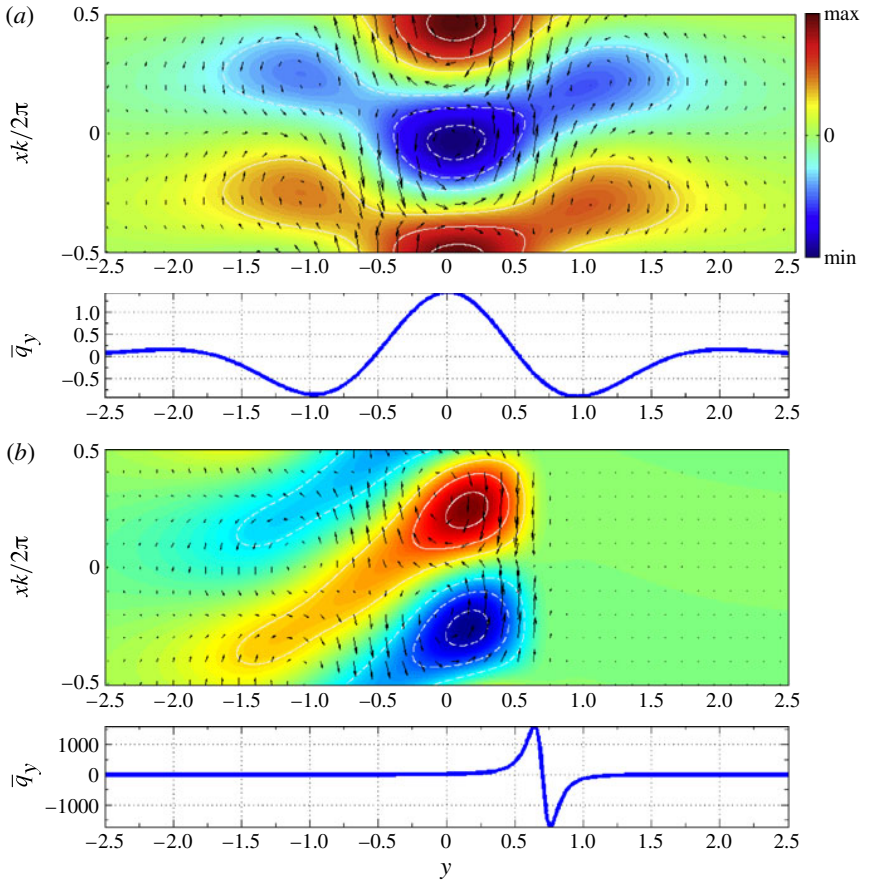


FIGURE 7. (Colour online) The fluctuation fields of the B–B modes at $k = 1$ and the mean potential vorticity gradient $\overline{q}_y$ profiles for (*a*) $Ro = 0.1$, $Fr = 0.05$ and (*b*) $Ro = 1.0$, $Fr = 0.99$ in $j = 3$; h' is shown by the colour and white contours; u' and v' are shown by the black vector arrows. For h', red or solid contour implies positive, blue or dashed contour implies negative and green implies zero. The same colour code applies to all the colour plots of h' in subsequent figures.

We see multiple B–B modes for the mean flows. In $j = 3$, there are mainly three unstable B–B modes in the quasi-geostrophic regime. As Ro and Fr increase, the growth rate of a B–B mode decreases. For $Ro = 1.0$ and $Fr = 0.99$ (figure 3), two of the unstable B–B modes almost vanish, and only the strongest mode remains (figure 7*b*). In $j = 1$ and 2, there are two unstable B–B modes in the small-Ro limit. (The two modes in $j = 1$ are also seen in Lambaerts *et al.* 2011.) For the Ro and Fr shown in figure 6, the small growth rate B–B mode no longer exists in $j = 1$. With the same finite Ro and Fr, both unstable B–B modes remain in the anticyclonic shear (figure 5) while only one remains with a very weak growth rate in the cyclonic shear (figure 4).

5. G–G and B–G instabilities

The G–G and B–G modes are unbalanced instabilities. Figure 8 shows an example of the fluctuation fields for the two types of mode in $j = 3$. The fluctuations have an

https://doi.org/10.1017/jfm.2012.422 Published online by Cambridge University Press

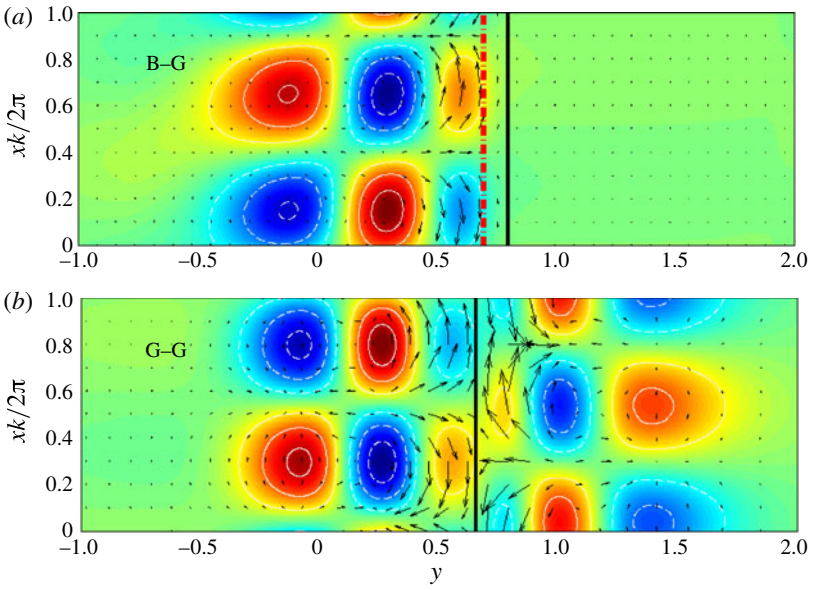


FIGURE 8. (Colour online) The fluctuation fields of (*a*) a B–G mode at $k = 2.83$ and (*b*) a G–G mode at $k = 4.52$ for $Ro = 1.0$, $Fr = 0.99$ and $j = 3$; h' is shown by the colour and white contours; u' and v' are shown by the black vector arrows. The straight black line indicates the critical layer where $\overline{u} = Cp$, and the red dot-dashed line indicates the inflection point where $\overline{q}_y = 0$.

inertia–gravity wave mode pattern in y for both types. All G–G and B–G unstable modes have critical layers (shown by the black straight lines in figure 8). For a G–G mode, there are two G components, distributed on each side of the critical layer. Only one G component appears in a B–G mode.

The G–G instability can be interpreted as a sharp resonance between two inertia–gravity wave modes from each group (N and P) respectively. The analytical dispersion relation for a G mode without the mean flow is shown in (3.6). With the existence of a mean flow background, dispersion relation curves are modified. Because the mean flow varies slowly, we assume the solution has a form $\mathrm{e}^{\mathrm{i}ly}$ in y to make a local estimation of the new dispersion relation for the two groups of G modes:

$$\hat{C}_p^{\pm} = \overline{u}^{\pm} \pm \sqrt{(k^2 + m^2)\left(\frac{1}{Fr^2} + \frac{\overline{h}^{\pm}}{Ro}\right) + \frac{1}{Ro^2}} \Big/ k, \tag{5.1}$$

where $\overline{u}^+$ or $\overline{u}^-$ is the local mean flow velocity, and $\overline{h}^+$ or $\overline{h}^-$ is the associated local surface elevation. The values of $\overline{u}^+$, $\overline{u}^-$, $\overline{h}^+$, and $\overline{h}^-$ are constants, which can be obtained by averaging the $\overline{u}$ or $\overline{h}$ over the y region where the G component is located. Note that the meridional wavenumber is represented by m in this new dispersion relation. Without the mean flow, the meridional wavenumber l is continuous, while with the mean flow, only integer and half-integer meridional wavenumbers are allowed, so we change to the notation m. Four C_p curves of each group (in red and blue, respectively) calculated from (3.6) are shown in figure 9(*a*). They are the dispersion curves for the free G modes without the mean flow. Figure 9(*b*) shows the mean

https://doi.org/10.1017/jfm.2012.422 Published online by Cambridge University Press

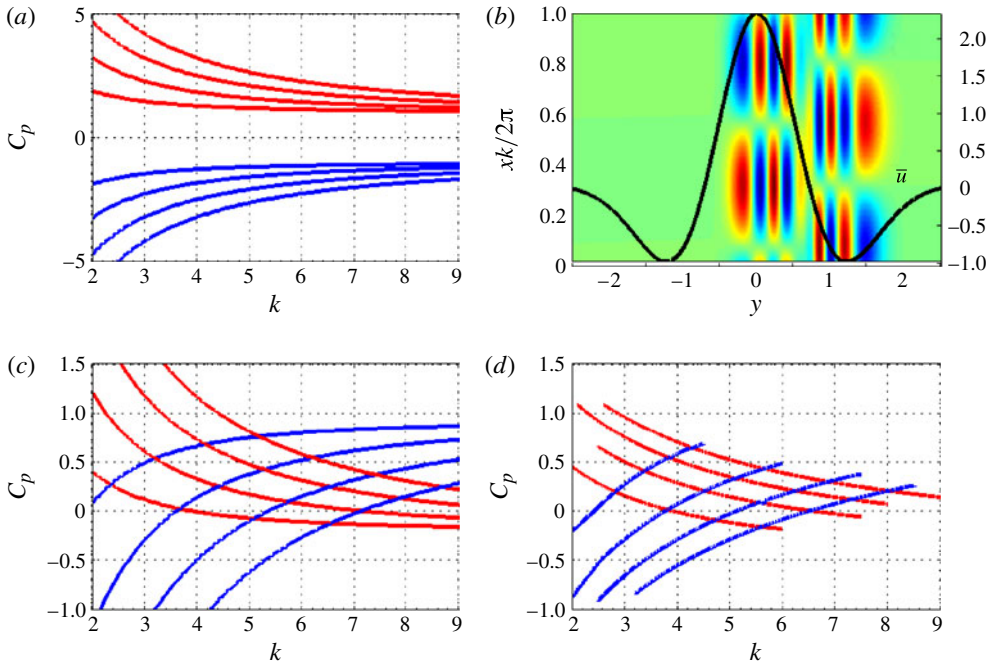


FIGURE 9. (Colour online) An explanation of the G–G resonance by C_p for $Ro = 1.0$, $Fr = 0.99$ and $j = 3$. (*a*) The C_p curves of a few neutral G modes without mean flow. (*b*) The fluctuation h' (in colour) of a G–G mode at $k = 8.01$, with the background mean flow superimposed (black curve, right axis). (*c*) The C_p curves with the modification by the local mean flow calculated from (5.1) (see text). (*d*) The same C_p curves as (*c*), except that they are obtained from the numerical eigensolver.

flow and the fluctuation h' for a resonant G–G mode in $j = 3$, as a function of y. The fluctuation has two G components: the left one ($y < 0.8$), in the N group, is concentrated in the positive-signed $\overline{u}$ region, and the right one ($y > 0.8$), in the P group, is concentrated in the negative-signed $\overline{u}$ region. With the Doppler shift and modification by the mean flow, the P group is negatively shifted and the N group is positively shifted, leading to a cross of a pair of G mode C_p curves. When the two G modes have the same phase speed, they can resonate with each other, and instability occurs. The $\hat{C}_p^{\,+}$ and $\hat{C}_p^{\,-}$ estimated from (5.1) are shown in figure 9(*c*). They agree well with the C_p obtained by the eigensolver in figure 9(*d*). Figure 10 shows an example of the G–G resonance. The plots in figure 10(*a*) are the growth rate and phase speed curves, magnified in the P_2–N_2 resonant peak region. Figure 10(*b*) shows the fluctuation h' of the unstable resonant mode (A) and its component G modes (B and C), respectively. When the C_p curves separate, the two G modes are almost stable, and only one G mode appears in the fluctuation pattern. When the curves overlap, the growth rate appears as a peak and the fluctuation pattern contains both G components.

Rather than having a sharp resonant peak in the growth rate, the B–G modes occur over a wide k range in between the B–B modes and the G–G modes. We interpret an unstable B–G mode as a result of the interaction between a B mode and a G mode. The fluctuation of the unstable mode is highly ageostrophic, and its growth rate vanishes for a small Ro and Fr. The G component appears in the y region where the local $\overline{u}$ is opposite-signed to the phase speed of the free neutral G mode. As discussed

https://doi.org/10.1017/jfm.2012.422 Published online by Cambridge University Press

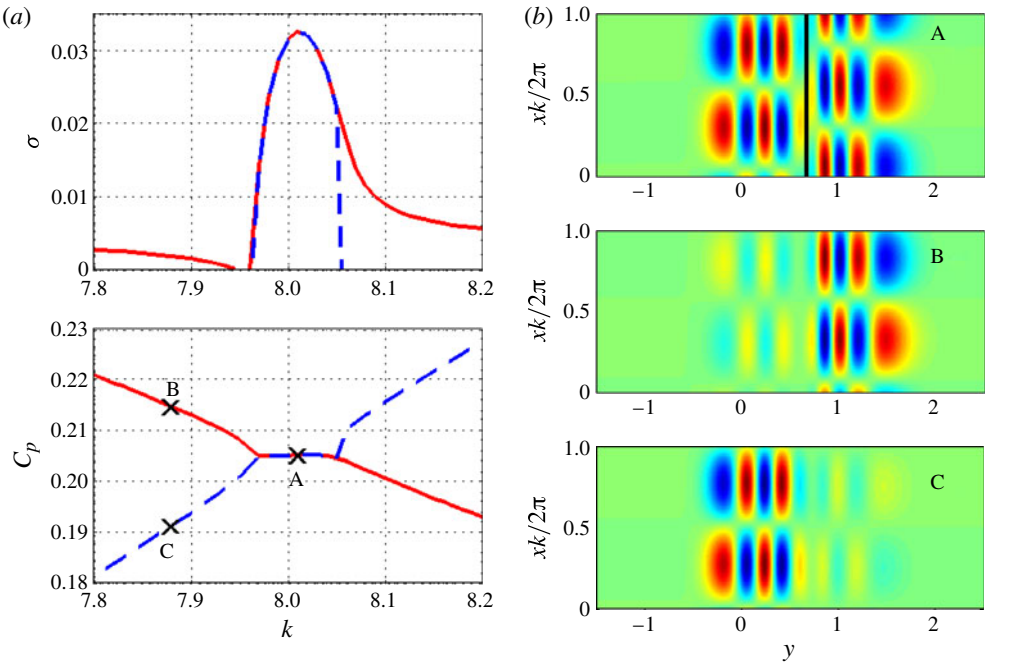


FIGURE 10. (Colour online) (*b*) Fluctuations h' for an unstable G–G mode (P_2–N_2) (A) at $k = 8.01$ (with the black line indicating the critical layer) and its neighbouring component G modes: a weakly unstable P_2 mode (B) and a neutral N_2 mode (C) at $k = 7.88$, for $Ro = 1.0$, $Fr = 0.99$, and $j = 3$. (*a*) Close-up of the growth rate and phase speed curves around $k = 8.01$.

in § 3, the neutral G mode is a fast mode and the neutral B mode is a slow mode; they are well separated without the background mean flow. With the Doppler shift of the mean flow and a finite *Ro* and *Fr*, the phase speed of the G mode becomes small, and thus able to interact with a slow B mode. Because all our mean flows have continuous, non-uniform $\overline{q}_y$, many B modes within a continuous range of phase speed values coexist and might resonate with the G mode. Therefore, we cannot identify a particular B component (in contrast to the G component in B–G and G–G instabilities). The pattern imprint of the G component is clear while that of the B component is obscure in the eigenfunctions for a large growth rate B–G mode (figure 8), though we do see the imprint of the B component in weakly unstable B–G modes (not shown), where the coupling of the B and G modes is not strong. For special shallow water flows with a singular $\overline{q}_y$ (Kubokawa 1986; Boss *et al.* 1996; Dritschel & Vanneste 2006; Gula & Zeitlin 2010), the B component is a distinct mode and has an identifiable pattern imprint trapped near the singular point. However, with our continuous, smooth $\overline{q}_y$, the B component is less evident in the unstable mode. The obscurity of the B component is also found in Balmforth (1999) in a flow without rotation. We have seen in other shallow water flows that the imprint of the B component in the unstable eigenmode fades as $\overline{q}$ changes from stepwise uniform to continuously non-uniform. Dritschel & Vanneste (2006) also report significant changes in the behaviour of the shear wave when $\overline{q}$ is smoothed over the front.

Both the G and B components are close to where $\overline{q}_y = 0$ (indicated by a red dot-dashed line in figure 8, and the $\overline{q}_y$ profile for this mean flow is shown in figure 7*b*),

https://doi.org/10.1017/jfm.2012.422 Published online by Cambridge University Press

but they are located at different sides of $\overline{q}_y = 0$. For instance in figure 8, the G component has a negative phase speed without the mean flow and it appears in the y region where $\overline{u}$ is positive, so the magnitude of its phase speed becomes a smaller negative value with the Doppler shift according to (5.1). The B component occurs in the y region where $\overline{q}_y$ is negative, which yields a positive phase speed, and the local $\overline{u}$ is negative, so the phase speed becomes a small negative value from the estimation (3.4). This is a consistent explanation for how the B and G modes resonate and lead to an instability. A similar explanation applies to all the B–G instabilities in $j = 1, 2$ and 3.

The four types of mean flow behave differently in ageostrophic instabilities (as shown in figures 3–6). In the Bickley jet ($j = 1$), we can only find the B–G instability. This is because the Bickley jet does not have both $\overline{u} > 0$ and $\overline{u} < 0$. The phase speed of the two groups of G modes cannot be shifted in the opposite direction to reach $\hat{C}_p{}^{+} = \hat{C}_p{}^{-}$. Although the $j = 2$ flows have both positive and negative $\overline{u}(y)$, the ageostrophic instability is significantly different. For moderate Ro and Fr, the cyclonic shear has both a G–G mode and a B–G mode, while we do not find G–G modes in the anticyclonic shear. The G–G instability occurs in $j = 2$ (anticyclonic) only for a Ro value over 10. According to (5.1), with the local $\overline{u}$ having the same magnitude, the phase speed of the G mode depends on the local $\overline{h}$. The cyclonic shear has a negative $\overline{h}$, so it has a smaller phase speed magnitude than the anti-cyclonic shear. Therefore, the G–G instability is more likely to occur in the cyclonic shear than in the anticyclonic shear.

6. Ro and Fr dependence, degree of ageostrophy and energy diagnostics

6.1. *Ro and Fr dependence*

For an intermediate Ro and Fr, the balanced modes (B–B) and ageostrophic modes (B–G and G–G) coexist in our mean flows, occurring at different spatial scales. As Ro, $Fr \to 0$, only the B–B instability occurs. As Ro and Fr increase, the ageostrophic instability begins to appear. In this section we address two questions: (i) In what Ro and Fr regime does the ageostrophic instability begin to appear? (ii) As Ro and Fr increase, how does the growth rate of the balanced and ageostrophic instabilities change?

Ripa (1983) derived two sufficient stability conditions for a shallow water parallel flow: if there exists any constant value of α such that

$$(\alpha - \overline{u}(y))\frac{\mathrm{d}\overline{q}(y)}{\mathrm{d}y} \geqslant 0 \tag{6.1}$$

and

$$Fr^2\,(\alpha - \overline{u}(y))^2 \leqslant 1 + \frac{Fr^2}{Ro}\overline{h}(y) \tag{6.2}$$

for all y, then the flow is stable to infinitesimal perturbations. In other words, if for all α one of the conditions is violated at some y, the flow may be unstable. The first condition is associated with Rayleigh's inflection-point condition, and is familiar in classical barotropic instability. The second condition refers to a local Froude number $\tilde{Fr}(y)$ defined by

$$\tilde{Fr}(y) = Fr\frac{|\overline{u}(y)|}{\sqrt{1 + \dfrac{Fr^2}{Ro}\overline{h}(y)}}. \tag{6.3}$$

https://doi.org/10.1017/jfm.2012.422 Published online by Cambridge University Press

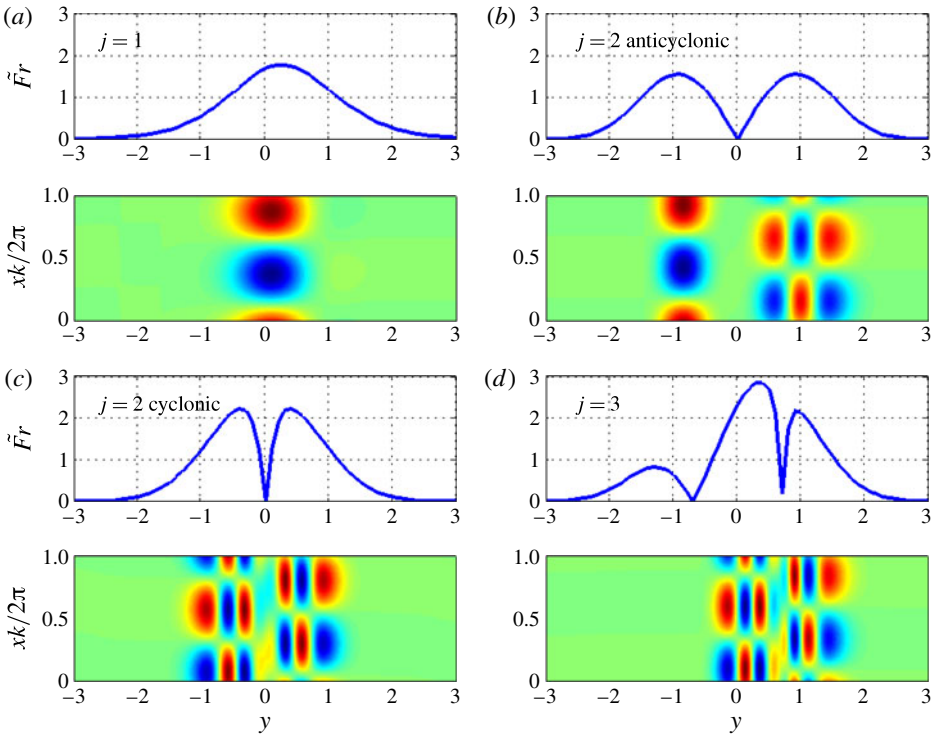


FIGURE 11. (Colour online) The local $\tilde{Fr}(y)$ for the mean flows (above) and the associated h' field (below) for the unstable ageostrophic modes: (*a*) $j = 1$, $Ro = 1.0$, $Fr = 0.50$; (*b*) $j = 2$ (anticyclonic), $Ro = 1.0$, $Fr = 2.50$; (*c*) $j = 2$ (cyclonic), $Ro = 1.0$, $Fr = 0.70$; (*d*) $j = 3$, $Ro = 1.0$, $Fr = 0.99$. A G–G mode is chosen in $j = 2$ and 3, and a B–G mode is chosen in $j = 1$.

Instability occurs when the local $\tilde{Fr}(y)$ is large enough (not the bulk Fr). Note that if taking $\alpha = 0$, (6.2) implies that the flow is stable when $\tilde{Fr} \leqslant 1$. However, because (6.2) is a sufficient condition and α could be any constant value, the real critical $\tilde{Fr}$ for the occurrence of the ageostrophic instability is not exactly 1 (figure 12). $\tilde{Fr}$ represents the local ratio of the strength of mean flow to that of the inertia–gravity wave speed, taking into account the surface elevation effect. For the occurrence of a G–G mode or a B–G mode, the G mode has to be Doppler-shifted by an opposite-signed local $\overline{u}$ (§ 5). To have an effective Doppler shift, the mean flow velocity should be comparable to the phase speed of a free G mode, which requires a local $\tilde{Fr}$ of order one.

Figure 11 shows the relation between $\tilde{Fr}(y)$ and the eigenmode patterns for the four types of mean flow. (One example is shown for each flow.) The fluctuation field is concentrated in the y region where the local $\tilde{Fr}(y)$ is larger than a critical value and decays outside that region for all the ageostrophic unstable modes in the mean flows. As shown in figure 11, for the same Ro (1.0) and bulk Fr (0.7), the local $\tilde{Fr}$ is different in $j = 2$ flows. Due to the surface elevation effect, the cyclonic shear has a larger local $\tilde{Fr}$ than the anticyclonic shear, which implies that the occurrence of an ageostrophic instability requires a larger Ro and bulk Fr in the anticyclonic shear flow (§ 5). With the assumption $(u', v', h') = \mathrm{Re}[(\hat{u}(y), \hat{v}(y), \hat{h}(y))\, \mathrm{e}^{\mathrm{i}(kx-\omega t)}]$ (§ 2),

https://doi.org/10.1017/jfm.2012.422 Published online by Cambridge University Press

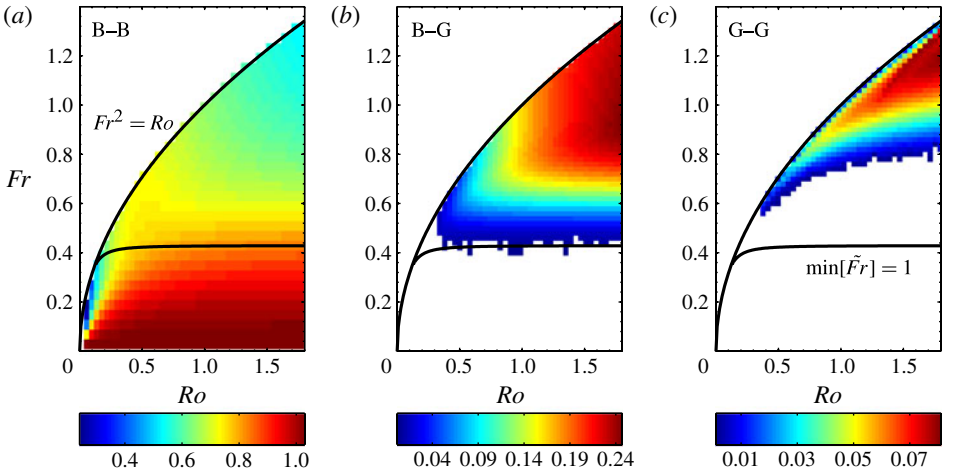


FIGURE 12. The σ values in the (Fr, Ro) space for the three types of unstable modes (B–B, B–G and G–G) in $j = 3$. The upper solid black curve $Fr^2 = Ro$ shows the limits for the existence of a geostrophic mean flow. The lower black line is the contour for $\min[\tilde{Fr}(y)] = 1$. For the B–B and B–G modes, we choose the maximum growth rate for each Ro and Fr. For the G–G mode, we choose the maximum growth rate of a particular mode $P_{1.5}$–N_1. We have checked and confirmed that other G–G modes behave the same as this one for the dependence of Ro and Fr.

the fluctuation (2.4) can be simplified to a second-order differential equation in y: $\mathrm{d}^2\eta/\mathrm{d}y^2 + \chi(y)(\mathrm{d}\eta/\mathrm{d}y) + \gamma(y)\eta = 0$, where η could be either $\hat{u}$, $\hat{v}$ or $\hat{h}$. Neglecting the $\chi(y)(\mathrm{d}\eta/\mathrm{d}y)$ term (which is much smaller than the other two terms in our problem) and considering the behaviour of η locally, the sign of $\gamma(y)$ determines whether the solution oscillates or decays with y, and $\gamma(y)$ is approximately proportional to $\tilde{Fr}^2(y) - \phi(y)$ (the detailed derivation is not shown). When $\tilde{Fr}(y)$ is above a certain value, $\gamma(y) > 0$, the fluctuation has an oscillatory pattern where the unstable mode amplitude is large; when $\tilde{Fr}(y)$ is smaller than the threshold, $\gamma(y) < 0$, the magnitude of the fluctuation decays and disappears. This relates $\tilde{Fr}(y)$ to the edge of the unstable modes (shown in figure 11), and indicates that the existence of an unstable ageostrophic mode requires a sufficiently large local $\tilde{Fr}$.

Figure 12 shows the maximum growth rate in the (Ro, Fr) space for the B–B, B–G modes and a particular G–G mode ($P_{1.5}$–N_1), in $j = 3$. For B–B instability, the growth rate almost does not depend on Ro at a small Fr (<0.1), consistent with the classical barotropic instability of a two-dimensional fluid. For $Fr < 0.4$, the growth rate increases with increasing Ro, while for $Fr > 0.4$ the growth rate decreases slightly with increasing Ro. For a fixed Ro, the growth rate of B–B instability weakens significantly with increasing Fr, especially for small Ro. On the contrary, the ageostrophic instabilities (B–G and G–G) are more unstable for a larger Fr. The strongest growth rate of the ageostrophic instability appears just below the edge for the existence limit of a geostrophic mean flow (indicated by the upper black line; § 2). The B–G instability is stronger than the G–G instability, and starts to appear at a lower Fr value than the G–G instability. The line $\min[\tilde{Fr}(y)] = 1$ is plotted by the lower black curve. The two black lines roughly enclose the regime for the B–G instability.

https://doi.org/10.1017/jfm.2012.422 Published online by Cambridge University Press

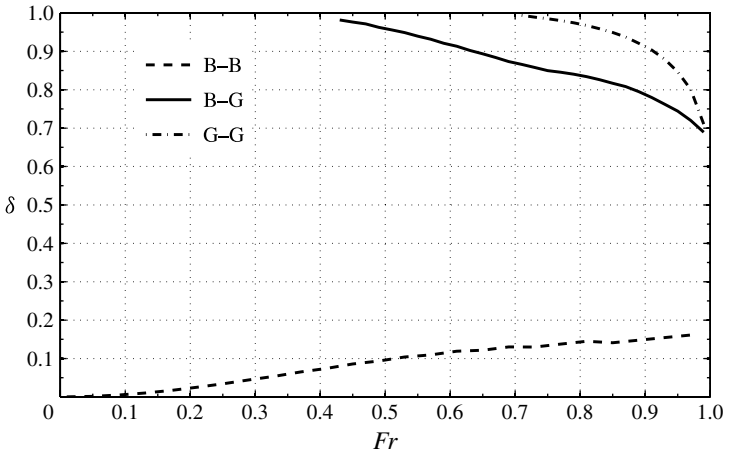


FIGURE 13. The ratio of the divergent component in fluctuation velocity $\delta = \|\boldsymbol{u}'_{div}\|/\|\boldsymbol{u}'\|$ for the B–B, B–G and G–G modes in $j = 3$, for a fixed $Ro = 1.0$. The same unstable modes as in figure 12 are chosen to calculate this ratio.

Although not shown in figure 12(*c*), the line $\min[\tilde{Fr}(y)] = 1.7$ roughly marks the lower limit of the G–G instability. This confirms that the ageostrophic instabilities are associated with the violation of Ripa's second condition. For intermediate Ro and Fr (order one) in $j = 3$, the growth rate of ageostrophic modes is small compared with the balanced mode. However, with increasing Ro and Fr, the growth rate of the balanced instability decreases, while that of the ageostrophic instability increases. At large Ro and Fr, the ageostrophic instability would be stronger than the balanced instability. The relative strength of the three instabilities varies significantly for different types of flow. For instance, in $j = 2$ (cyclonic), the B–G ageostrophic instability is the most unstable one among the three instabilities for $Ro = 1.0$ and $Fr = 0.70$ (figure 4), i.e. the ageostrophic instability is dominant over the balanced instability. In contrast, the balanced instability is dominant in $j = 2$ (anticyclonic) and the Bickley jet for $Ro = 1.0$.

6.2. *Degree of ageostrophy*

Besides the difference in the growth rate dependence on Fr, the balanced instability and ageostrophic instability have a significant difference in the degree of ageostrophy for the eigenmodes. We use the divergent component of the fluctuation velocity to represent the degree of ageostrophy, which is defined as

$$\delta = \frac{\|\boldsymbol{u}'_{div}\|}{\|\boldsymbol{u}'\|} = \sqrt{\frac{\int \left(\overline{u'^2_{div}} + \overline{v'^2_{div}}\right)\,\mathrm{d}y}{\int \left(\overline{u'^2} + \overline{v'^2}\right)\,\mathrm{d}y}}. \tag{6.4}$$

The divergent velocity is evaluated by $\boldsymbol{u}'_{div} = \boldsymbol{u}' - \boldsymbol{u}'_{geo}$, where $\boldsymbol{u}'_{geo} = \hat{\boldsymbol{z}} \times \nabla\psi'$. The vorticity of the fluctuation is the same as the geostrophic component: $\zeta' = \hat{\boldsymbol{z}}\cdot(\nabla \times \boldsymbol{u}') = \hat{\boldsymbol{z}} \cdot (\nabla \times \boldsymbol{u}'_{geo}) = \nabla_h^2\psi'$, and we obtain ψ' by $\psi' = \nabla_h^{-2}\zeta'$. We plot δ versus Fr for the three instabilities for fixed $Ro = 1.0$ in figure 13. The B–B eigenmode has a zero divergent component at small Fr. Although the divergent part increases with Fr, it

https://doi.org/10.1017/jfm.2012.422 Published online by Cambridge University Press

remains small for a broad range of finite Fr. With a finite Ro and Fr effect, the mode is still balanced (§§ 3.1 and 4). For B–G and G–G modes, the divergent velocity is dominant, indicating that the fluctuation is highly ageostrophic. When the ageostrophic instability starts to appear at the critical Fr (roughly 0.4 for B–G and 0.7 for G–G), the growth rate is weak and the mode is mostly a neutral G mode that is not coupled with the mean shear, so the fluctuation is almost purely divergent ($\delta \sim 1$). When Fr increases, the mean flow interacts with the G mode, leading to unstable modes. The unstable mode is not purely divergent due to the participation of the mean flow. The B–G mode involves the interaction between a B mode and a G mode, so the ageostrophic degree is smaller than a G–G mode. Although the result is shown for a fixed $Ro = 1.0$, the conclusion discussed above remains the same for different Ro cases. The higher-order balance for the instabilities is not checked in our work. However, because both the B–G and G–G instabilities clearly involve a coupling with inertia–gravity waves, they are unbalanced instabilities.

6.3. *Energy diagnostics*

To reach a more complete view of the unstable modes, the energetics is examined. In the linearized shallow water system, we express the total energy E as the sum of the mean energy $\overline{E}$ and the quadratic fluctuation energy E':

$$\overline{E} = \int \left[\frac{1}{2}\left(1 + \frac{Fr^2}{Ro}\overline{h}\right)\overline{u}^2 + \frac{1}{2}\frac{Fr^2}{Ro^2}\overline{h}^2 + \frac{1}{Ro}\overline{h}\right] \mathrm{d}y, \tag{6.5}$$

$$E' = \int \left[\frac{1}{2}\left(1 + \frac{Fr^2}{Ro}\overline{h}\right)(\overline{u'^2} + \overline{v'^2}) + \frac{1}{2}\frac{Fr^2}{Ro^2}\overline{h'^2} + \frac{Fr^2}{Ro}\overline{u}\overline{h'u'}\right] \mathrm{d}y, \tag{6.6}$$

where the overbar denotes the zonal average. The total energy $E = \overline{E} + E'$ is conserved without viscosity. The energy balance for the mean flow and the fluctuations is given by

$$\frac{\mathrm{d}E'}{\mathrm{d}t} = \int \left[\left(1 + \frac{Fr^2}{Ro}\overline{h}\right)\overline{u}\overline{v'}\overline{\frac{\partial u'}{\partial y}} - \frac{Fr^2}{Ro^2}\overline{h'v'}\left(Ro\overline{u}\frac{\partial \overline{u}}{\partial y} + \frac{\partial \overline{h}}{\partial y}\right)\right] \mathrm{d}y, \tag{6.7a}$$

$$\frac{\mathrm{d}\overline{E}}{\mathrm{d}t} = \int \left[-\left(1 + \frac{Fr^2}{Ro}\overline{h}\right)\overline{u}\overline{v'}\overline{\frac{\partial u'}{\partial y}} + \frac{Fr^2}{Ro^2}\overline{h'v'}\left(Ro\overline{u}\frac{\partial \overline{u}}{\partial y} + \frac{\partial \overline{h}}{\partial y}\right)\right] \mathrm{d}y. \tag{6.7b}$$

The first conversion term is related to the horizontal Reynolds stress (as in classical barotropic instability), and the second is related to eddy mass flux (Stokes drift).

The ratio of potential to kinetic energy of the fluctuations PE/KE is examined, where $PE = \int (Fr^2/2Ro^2)\overline{h'^2}$ and $KE = \int (1 + (Fr^2/Ro)\overline{h})/2(\overline{u'^2} + \overline{v'^2})$. KE is dominant for all three types of instability. The PE/KE ratio is larger in the ageostrophic instabilities than in the balanced instability. For the conversion between $\overline{E}$ and E', the first and second terms in (6.7) have the same sign in the balanced instability, but have opposite signs in the ageostrophic ones, implying that the ageostrophic unstable fluctuations transfer energy to the mean flow through the mass fluxes. The first conversion term, horizontal Reynolds stress, is dominant for all three types of instability.

7. A nonlinear example of ageostrophic instability: modon

In $j = 2$ (cyclonic), the ageostrophic instability is dominant over the balanced instability for intermediate Ro and Fr values. Compared with the cyclonic case, the balanced instability is stronger, and the ageostrophic instability is weaker for $j = 2$

https://doi.org/10.1017/jfm.2012.422 Published online by Cambridge University Press

(anticyclonic), with the same Ro and Fr. This asymmetry is also seen in $j = 3$, where the balanced instability appears in the region with negative potential vorticity, and the ageostrophic instability appears in the region with positive potential vorticity and large local $\tilde{Fr}$. Therefore, in the nonlinear time evolution of a rotating shallow water flow for a finite Ro and Fr, it is expected that the ageostrophic instability would appear in a cyclone. This expectation is borne out in the time evolution of a modon for finite Ro.

A modon, as studied by McWilliams (1981) and Kizner *et al.* (2008), is a steadily propagating dipole. The steady modon solution for $Ro = 0.2$ and $Fr = 0.2$ in Kizner *et al.* (2008) is taken to be the initial condition for the time-integration study of the nonlinear shallow water equations (2.1). The surface elevation h, potential vorticity q, and local $\tilde{Fr}$ of the modon solution are shown in figure 14(*a*), where

$$q = \frac{1 + Ro(v_x - u_y)}{1 + \dfrac{Fr^2}{Ro}h}, \qquad \tilde{Fr} = Fr\frac{|\boldsymbol{u}|}{\sqrt{1 + \dfrac{Fr^2}{Ro}h}}. \tag{7.1}$$

Note that here u, v, h and q are non-dimensional variables. The y profiles at $x = 0$ are shown in figure 14(*b*). In order for the modon to steadily propagate, the strength of the cyclone and that of the anticyclone are quite asymmetric in h and q for finite Ro. The extremes of the cyclone are stronger than those of the anticyclone. Unlike the symmetric parallel flows studied in previous sections, the asymmetric modon profile leads to a sizable local $\tilde{Fr}$, even with relatively small bulk Ro and Fr.

The time evolution of the ageostrophic instability is shown in figure 14(*c*). The thick black lines in the third plot of figure 14(*a*) and in figure 14(*c*) circle the region where $\tilde{Fr}$ is larger than 1. The plots for the moving-frame modon are magnified in the cyclone region, which is indicated by the white rectangles in figure 14(*a*). The ageostrophic unstable waves are trapped in the cyclone region; as they evolve, they change the shape of the modon, evidently to make it less unstable, and then die away through viscosity. As circled by the thick black lines, the instability appears where the local $\tilde{Fr}$ is large, which is consistent with Ripa's second condition. The evolution of initial modons with smaller Ro and local $\tilde{Fr}$ does not manifest this spontaneous instability.

A linear instability analysis of a modon cross-section profile confirms the above nonlinear result. We take the y profile of h at $x = 0$ as the mean background $\overline{h}$, and calculate the $\overline{u}$ that is in geostrophic balance with $\overline{h}$. Note that $\overline{u}$ is different from the y profile of u at $x = 0$ of the modon. The $\overline{h}$ and $\overline{u}$ profiles are shown in figure 15(*a*). To be consistent with the nonlinear simulation, we take $Ro = 0.2$ and $Fr = 0.2$ in the linear calculation. We find multiple ageostrophic unstable modes in a range of intermediate and large k. The growth rate is significantly large compared to the symmetric idealized flows in previous sections (figure 15*b*). The k range (5–10) shown in the plot is consistent with the zonal length scale of the trapped ageostrophic instability occurring in the nonlinear evolution (figure 14*c*). The local $\tilde{Fr}(y)$ of the mean flow and an example of the unstable eigenmodes are shown in figure 15(*c*). The ageostrophic mode is trapped in the region where $\tilde{Fr}$ is the largest in y, which is consistent with the meridional position of its occurrence in the nonlinear evolution.

This modon example illustrates the transient, nonlinear behaviour of an ageostrophic instability in a more complex (non-parallel) flow. The time evolution of a finite Ro modon is also examined by Ribstein, Gula & Zeitlin (2010), where the ageostrophic instability is not observed, perhaps due to a lower resolution compared to our

https://doi.org/10.1017/jfm.2012.422 Published online by Cambridge University Press

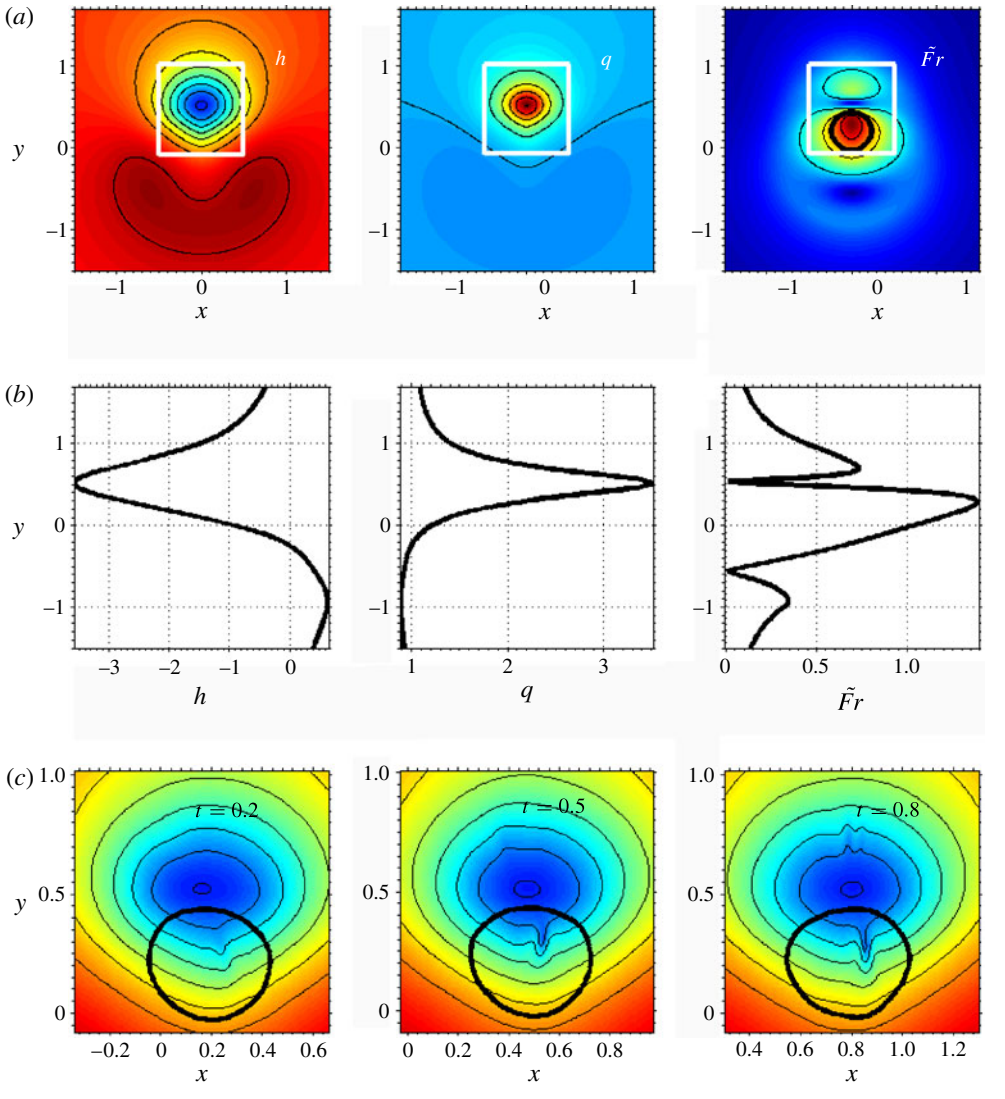


FIGURE 14. (Colour online) (*a,b*) The modon initial condition and (*c*) time evolution for $Ro = 0.2$ and $Fr = 0.2$ in the non-dimensional, nonlinear rotating shallow water equations. (*a*) The patterns for h, q and $\tilde{Fr}$ at $t = 0$: for h contours, the interval is 0.5 and the minimum value is -3.5 (the zero contour is not shown); for q contours, the interval is 0.5 and the minimum value is 0.5; for $\tilde{Fr}$ contours, the interval is 0.4 and the minimum value is 0.4. (*b*) $h(y)$, $q(y)$ and $\tilde{Fr}(y)$ at $x = 0$ and $t = 0$. (*c*) The patterns for h at $t = 0.2, 0.5$ and 0.8, respectively. The plot is magnified in the region indicated by the white rectangle in (*a*), following with the moving modon. The contours have the same values as in the h plot at $t = 0$. The thick black line circles where $\tilde{Fr} > 1$, both in the $\tilde{Fr}$ plot in (*a*) and the h plots in (*c*).

simulation. Lahaye & Zeitlin (2012) study the time evolution of a geostrophic modon in a higher Ro (0.3 or 0.4) shallow water model, and find shock formation during the adjustment process. We do not see similar phenomena in our simulation, perhaps because our initial condition is a steady modon solution to the finite Ro model and

https://doi.org/10.1017/jfm.2012.422 Published online by Cambridge University Press

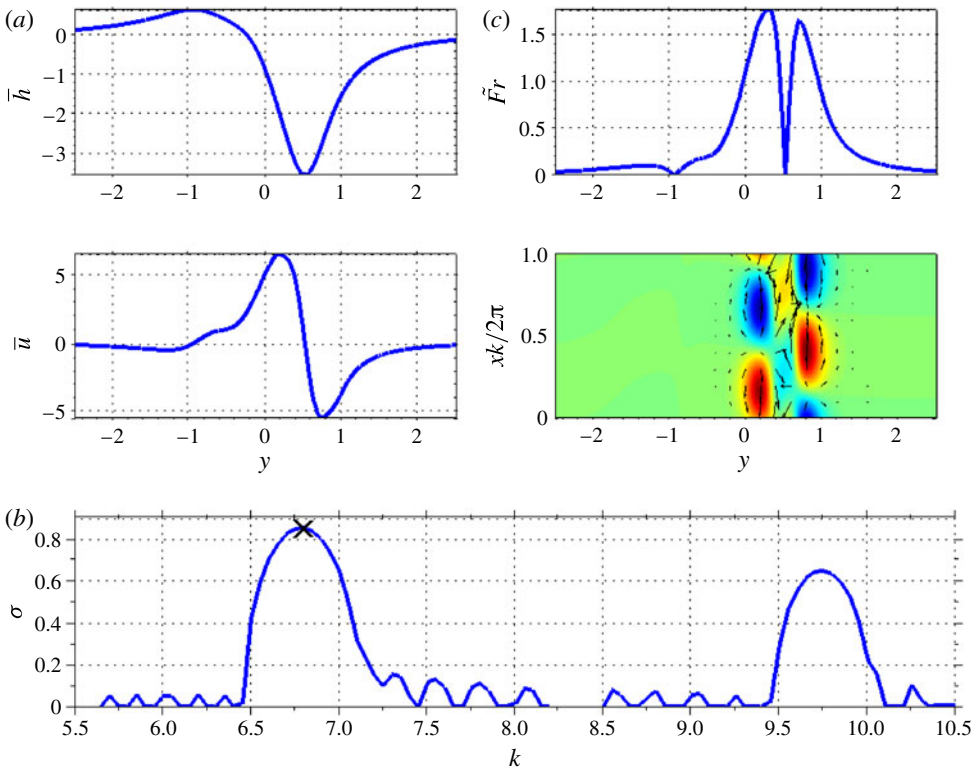


FIGURE 15. (Colour online) The linear instability analysis of the modon cross-section profile for $Ro = 0.2$ and $Fr = 0.2$. (*a*) The mean profile $\overline{h}(y)$ and $\overline{u}(y)$, where $\overline{h}$ is the cross-section of the steady modon profile at $x = 0$, and $\overline{u}$ is the zonal velocity in geostrophic balance with $\overline{h}$. (*b*) The growth rate σ versus k for multiple unstable ageostrophic modes. The selected k range is consistent with the length scale of the trapped instability appearing in the nonlinear evolution. (*c*) The local $\tilde{Fr}(y)$ and the fluctuation fields of an unstable ageostrophic mode for $k = 6.80$ (marked by a cross in the bottom σ plot). h' is shown by the colour; u' and v' are shown by the black vector arrows.

hence there is little adjustment. Furthermore, the Ro in our case (=0.2) might be too small for the occurrence of a shock.

8. Summary and discussion

To identify a general route for the breakdown of balance and the energy transfer towards small scales, the ageostrophic instability of a horizontal interior shear flow is studied in this paper. We solve for the instabilities in several balanced parallel shear flows $\overline{u}(y)$ (Bickley jet, cyclonic and anticyclonic double jet, and triple jet), with continuous, non-uniform potential vorticity, without side boundaries or vanishing layer depth, in a single-layer f-plane rotating shallow water model. In the system, there are mainly two types of neutral modes: B mode and G mode. A neutral B mode is a balanced shear wave mode that exists due to the potential vorticity gradient. A neutral G mode is an inertia–gravity wave mode. The resonant coupling of two neutral modes yields three types of instability: B–B, B–G and G–G. B–B instability is the balanced shear instability (classical barotropic instability) that relates to Rayleigh's inflection

https://doi.org/10.1017/jfm.2012.422 Published online by Cambridge University Press

point condition. Both B–G and G–G are unbalanced instabilities, which are highly ageostrophic and occur when the local $\tilde{Fr}$ is sufficiently large (associated with Ripa's second stability condition). The resonant G component can be clearly identified in the ageostrophic instabilities. However, the B–G instability involves a set of B modes due to a continuously varying potential vorticity gradient, so its resonant B component is less evident in the unstable modes. The balanced instability is suppressed by large Fr, while the growth rate of the ageostrophic instability increases with increasing Fr. For moderate Ro and Fr, all three types of instability appear in the cyclonic double jet and the triple jet, but only B–B and B–G instabilities appear in the anticyclonic double jet and the Bickley jet. The G–G instability can be found in the anticyclonic double jet for large Ro and Fr but never appears in the Bickley jet. In the cyclonic double jet, the ageostrophic instability is dominant over the balanced instability for intermediate Ro and Fr values. The ageostrophic instability is manifested in the nonlinear time evolution of a finite Ro modon, appearing in the cyclone region, where the local $\tilde{Fr}$ is large.

Our results show that ageostrophic instability is a generic behaviour for generic parallel, shallow water flows, not just ones with special boundaries or singular potential vorticity gradient. The occurrence of ageostrophic instability requires a large local $\tilde{Fr}$ and involves the interaction of at least one inertia–gravity wave with the mean flow. The unstable growth rate is a fraction of the mean shear rate, U/L, and its fractional magnitude varies with the particular mean flow shape.

As proposed in McWilliams *et al.* (1998), three criteria are related to the breakdown of balance in a three-dimensional flow, and they are associated with three types of instabilities. The N^2 (gravitational instability) and A (centrifugal instability) conditions do not apply to the single-layer shallow water model. They both involve vertical overturning in the unstable eigenmodes. The $A - S$ condition for the mean flow in the shallow water system is

$$\overline{A} - \overline{S} = 1 - Ro\overline{u}_y - Ro|\overline{u}_y|. \tag{8.1}$$

We check the critical Ro where $\min(\overline{A} - \overline{S})$ changes sign and find that it greatly precedes the onset of ageostrophic instabilities, and hence is not particularly relevant to shallow water instabilities, perhaps also because of the lack of overturning in the unstable modes. In contrast, Ripa's second stability condition is more relevant to the instability cases in the shallow water model. This suggests that the processes leading to loss of balance can be rather different in three-dimensional and shallow water fluids.

Acknowledgement

This research was partially supported by the US National Science Foundation (OCE-1049134) and Office of Naval Research (N00014-10-1-0484).

REFERENCES

BALMFORTH, N. J. 1999 Shear instability in shallow water. *J. Fluid Mech.* **387**, 97–127.

BOSS, E., PALDOR, N. & THOMPSON, L. 1996 Stability of a potential vorticity front: from quasi-geostrophy to shallow water. *J. Fluid Mech.* **315**, 65–84.

BOUCHUT, F., RIBSTEIN, B. & ZEITLIN, V. 2011 Inertial, barotropic, and baroclinic instabilities of the Bickley jet in two-layer rotating shallow water model. *Phys. Fluids* **23**, 126601.

CHANDRASEKHAR, S. 1961 *Hydrodynamic and Hydromagnetic Stability*. Cambridge University Press.

DRAZIN, P. G. & REID, W. H. 1981 *Hydrodynamic Stability*. Cambridge University Press.

https://doi.org/10.1017/jfm.2012.422 Published online by Cambridge University Press

DRITSCHEL, D. G. & VANNESTE, J. 2006 Instability of a shallow-water potential-vorticity front. *J. Fluid Mech.* **561**, 237–254.

GRIFFITHS, R. W., KILLWORTH, P. D. & STERN, M. E. 1982 Ageostrophic instability of ocean currents. *J. Fluid Mech.* **117**, 343–377.

GULA, J., PLOUGONVEN, R. & ZEITLIN, V. 2009 Ageostrophic instabilities of fronts in a channel in a stratified rotating fluid. *J. Fluid Mech.* **627**, 485.

GULA, J. & ZEITLIN, V. 2010 Instabilities of buoyancy-driven coastal currents and their nonlinear evolution in the two-layer rotating shallow water model. Part 1. Passive lower layer. *J. Fluid Mech.* **659**, 69–93.

GULA, J., ZEITLIN, V. & BOUCHUT, F. 2010 Instabilities of buoyancy-driven coastal currents and their nonlinear evolution in the two-layer rotating shallow water model. Part 2. Active lower layer. *J. Fluid Mech.* **665**, 209–237.

HAYASHI, Y. Y. & YOUNG, W. R. 1987 Stable and unstable shear modes of rotating parallel flows in shallow waters. *J. Fluid Mech.* **184**, 477–504.

HELD, I. M. 1985 Pseudomomentum and the orthogonality of modes in shear flows. *J. Atmos. Sci.* **42**, 2280–2288.

KILLWORTH, P., PALDOR, N. & STERN, M. 1984 Wave propagation and growth on a surface front in a two-layer geostrophic current. *J. Mar. Res.* **42**, 761–785.

KIZNER, Z., REZNIK, G., FRIDMAN, B., KHVOLES, R. & MCWILLIAMS, J. 2008 Shallow-water modons on the f-plane. *J. Fluid Mech.* **603**, 305–329.

KUBOKAWA, A. 1985 Instability of a geostrophic front and its energetics. *Geophys. Astrophys. Fluid* **33**, 323–357.

KUBOKAWA, A. 1986 Instability caused by the coalescence of two modes of a one-layer coastal current with a surface front. *J. Oceanogr.* **42**, 373–380.

LAHAYE, N. & ZEITLIN, V. 2012 Shock modon: a new type of coherent structure in rotating shallow water. *Phys. Rev. Lett.* **108** (4), 044502.

LAMBAERTS, J., LAPEYRE, G. & ZEITLIN, V. 2011 Moist versus dry barotropic instability in a shallow-water model of the atmosphere with moist convection. *J. Atmos. Sci.* **68**, 1234–1252.

LIN, C. C. 1961 Some mathematical problems in the theory of the stability of parallel flows. *J. Fluid Mech.* **10**, 430–438.

MCWILLIAMS, J. 1981 Numerical studies of barotropic modons. *Dyn. Atmos. Oceans* **5**, 219–238.

MCWILLIAMS, J. C. 2003 Diagnostic force balance and its limits. *Nonlinear Process. Geophys. Fluid Dyn.* 287–304.

MCWILLIAMS, J. C. & MOLEMAKER, M. J. 2004 Ageostrophic, anticyclonic instability of a geostrophic, barotropic boundary current. *Phys. Fluids* **16**, 3720–3725.

MCWILLIAMS, J. C. & YAVNEH, I. 1998 Fluctuation growth and instability associated with a singularity of the balance equations. *Phys. Fluids* **10**, 2587–2596.

MCWILLIAMS, J. C., YAVNEH, I., CULLEN, M. J. P. & GENT, P. R. 1998 The breakdown of large-scale flows in rotating, stratified fluids. *Phys. Fluids* **10**, 3178–3184.

MÉNESGUEN, C., MCWILLIAMS, J. C. & MOLEMAKER, M. J. 2012 Ageostrophic instability in a rotating stratified interior jet. *J. Fluid Mech.* **711**, 599–619.

MOLEMAKER, M. J. & MCWILLIAMS, J. C. 2005 Baroclinic instability and loss of balance. *J. Phys. Oceanogr.* **35**, 1505–1517.

MOLEMAKER, M. J., MCWILLIAMS, J. C. & YAVNEH, I. 2001 Instability and equilibration of centrifugally stable stratified Taylor–Couette flow. *Phys. Rev. Lett.* **86**, 5270–5273.

OOYAMA, K. 1966 On the stability of the baroclinic circular vortex: a sufficient condition for instability. *J. Atmos. Sci.* **23**, 43–53.

PALDOR, N. 1983 Linear stability and stable modes of geostrophic fronts. *Geophys. Astrophys. Fluid* **24**, 299–326.

PERRET, G., DUBOS, T. & STEGNER, A. 2011 How large-scale and cyclogeostrophic barotropic instabilities favor the formation of anticyclonic vortices in the ocean. *J. Phys. Oceanogr.* **41**, 303–328.

POULIN, F. J. & FLIERL, G. R. 2003 The nonlinear evolution of barotropically unstable jets. *J. Phys. Oceanogr.* **33**, 2173–2192.

RAYLEIGH, LORD 1880 On the stability, or instability, of certain fluid motions. *Proc. Lond. Math. Soc.* **11**, 57–70.

https://doi.org/10.1017/jfm.2012.422 Published online by Cambridge University Press

RIBSTEIN, B., GULA, J. & ZEITLIN, V. 2010 (A)geostrophic adjustment of dipolar perturbations, formation of coherent structures and their properties, as follows from high-resolution numerical simulations with rotating shallow water model. *Phys. Fluids* **22**, 116603.

RIPA, P. 1983 General stability conditions for zonal flows in a one-layer model on the beta-plane or the sphere. *J. Fluid Mech.* **126**, 463–489.

SAKAI, S. 1989 Rossby–Kelvin instability: a new type of ageostrophic instability caused by a resonance between Rossby waves and gravity waves. *J. Fluid Mech.* **202**, 149–176.

SATOMURA, T. 1980 An investigation of shear instability in a shallow water. *J. Met. Soc. Japan* **59**, 148.

YAVNEH, I., MCWILLIAMS, J. C. & MOLEMAKER, M. J. 2001 Non-axisymmetric instability of centrifugally stable stratified Taylor–Couette flow. *J. Fluid Mech.* **448**, 1–21.

https://doi.org/10.1017/jfm.2012.422 Published online by Cambridge University Press